Search for the Skyrme-Hartree-Fock solutions for chiral rotation in $N = 75$ isotones

P. Olbratowski,[1,*] J. Dobaczewski,[1,†] and J. Dudek[2,‡]

[1]*Institute of Theoretical Physics, Warsaw University, ul. Hoża 69, PL-00681, Warsaw, Poland*
[2]*Institut de Recherches Subatomiques IN₂P₃-CNRS/Université Louis Pasteur, F-67037 Strasbourg Cedex 2, France*

A search for self-consistent solutions for the chiral rotational bands in the $N = 75$ isotones ^{130}Cs, ^{132}La, ^{134}Pr, and ^{136}Pm is performed within the Skyrme-Hartree-Fock cranking approach using SKM* and SLy4 parametrizations. The dependence of the solutions on the time-odd contributions in the energy functional is studied. From among the four isotones considered, self-consistent chiral solutions are obtained only in ^{132}La. The microscopic calculations are compared with the ^{132}La experimental data and with results of a classical model that contains all the mechanisms underlying the chirality of the collective rotational motion. Strong similarities between the Hartree-Fock and classical model results are found. The suggestion formulated earlier by the authors that the chiral rotation cannot exist below a certain critical frequency is further illustrated and discussed, together with the microscopic origin of a transition from planar to chiral rotation in nuclei. We also formulate the separability rule by which the tilted-axis-cranking solutions can be inferred from three independent principal-axis-cranking solutions corresponding to three different axes of rotation.

PACS number(s): 21.30.Fe, 21.60.Ev, 21.60.Jz, 27.60.+j

I. INTRODUCTION

Since the original 1997 work of Frauendorf and Meng [1], the phenomenon of chiral rotation in atomic nuclei has attracted significant attention. The effect is expected to occur in nuclei having stable triaxial deformation, and in which there are a few high-j valence particles and a few high-j valence holes. The former drive the nucleus toward prolate shapes, and the latter toward oblate shapes. The interplay of these opposite tendencies may favor a stable triaxial deformation. For such a shape, the valence particles and holes align their angular momenta along the short and long axes of the density distribution, respectively. However, the nuclear-bulk moment of inertia with respect to the medium axis is the largest, which favors collective rotation about that axis. Thus, the particle, hole, and collective angular momentum vectors are aplanar and may form either a left-handed or a right-handed set. In this way, the two enantiomeric forms may give rise to pairs of rotational bands, which are called chiral doublets. It is expected that the energy splitting between the partners in such doublets is very small, and in fact the authors of Ref. [2], who have analyzed the experimental results, have used essentially the argument "by elimination"—the bands were suggested to be chiral partners mainly because their properties could not be explained within other scenarios used by the authors.

The first doublet band, later reinterpreted as chiral [1], was found in 1996 by Petrache *et al.* in ^{134}Pr [3]. Now, about 15 candidate chiral doublet bands are known in the $A \approx 130$ region, and about 10 in the $A \approx 100$ region. Most bands in the $A \approx 130$ nuclei are assigned to the simplest chiral configuration, with one proton particle on the $\pi h_{11/2}$ orbital, and one neutron hole on the $\nu h_{11/2}$ orbital. Configurations for $A \approx 100$ nuclei usually involve one $\pi g_{9/2}$ proton hole and

one $\nu h_{11/2}$ neutron particle orbitals. A few cases with more than one active particle or hole were also found [4–6]. So far, experimental information about absolute $B(E2)$ and $B(M1)$ values for transitions within the observed bands is available only for ^{128}Cs and ^{132}La from recent lifetime measurements by Grodner [7,8] and Srebrny [9] and collaborators.

On the theoretical side, chiral rotation has been extensively studied by using various versions of the particle-rotor model (PRM) (see, e.g., Refs. [10–12]). In PRM, the nucleus is represented by the valence particles and holes coupled via the quadrupole-quadrupole interaction to a rotator, often described within the Davydov-Filippov model [13] with moments of inertia given by the irrotational-flow formula [14]. However, the main concept of rotational chirality summarized here, came from considerations within the Frauendorf's mean-field tilted-axis-cranking (TAC) model [15–17], which is used in parallel with the PRM. That model is a straightforward generalization of the standard cranking approach to situations where the axis of rotation does not coincide with any principal axis of the mass distribution. The first chiral TAC solution for a fixed triaxial shape was obtained in 1987 by Frisk and Bengtsson [18] and then in 1997 by Frauendorf and Meng [1,19]. In 2000, Dimitrov, Frauendorf, and Dönau [20] obtained the first such solution by minimizing the energy over deformation. From the TAC results, Frauendorf [21,22] and Dimitrov and collaborators [23] reproduced or predicted the chiral rotation in several nuclei from the 130 and 100 mass regions, and also in ^{79}Br, ^{162}Tm, and ^{188}Ir. Other authors analyzed many experimental data within that approach [2,4–6,24,25], and generally a good correlation was found between the existence of chiral TAC solutions and the appearance of candidate chiral bands.

Up to now, all the TAC calculations for chiral rotation were based on simple model single-particle (s.p.) potentials [26] combined either with the pairing + quadrupole-quadrupole model (PQTAC) or the Strutinsky shell correction (SCTAC) [16]. A more fundamental description requires self-consistent

---

*Electronic address: Przemyslaw.Olbratowski@fuw.edu.pl
†Electronic address: Jacek.Dobaczewski@fuw.edu.pl
‡Electronic address: Jerzy.Dudek@ires.in2p3.fr

methods, which would provide a strong test of the stability of the proposed chiral configurations with respect to the core degrees of freedom. Self-consistent methods are also necessary to take into account the various kinds of polarization of the core by the valence particles and full minimization of the underlying energies with respect to all deformation degrees of freedom, including deformations of the current and spin distributions. Application of self-consistent methods to the description of chiral rotation is the subject of the present paper.

Our study concerns four $N = 75$ isotones, ^{130}Cs, ^{132}La, ^{134}Pr, and ^{136}Pm, which are the first nuclei in which candidate chiral bands were systematically studied [2]. We used the Hartree-Fock (HF) method with the Skyrme effective interaction. The results were obtained for two Skyrme parameter sets, SLy4 [27] and SkM* [28], and the role of terms in the mean field that are odd under time reversal was examined. Calculations were carried out by using a new version of the code HFODD (v2.05c) [29–31], which was specially constructed by the authors for the purpose of the present study. From among the four isotones considered, self-consistent chiral solutions were obtained in ^{132}La. A brief report on the results obtained in ^{132}La was given in Ref. [32].

The paper is organized as follows. In Sec. II we discuss some characteristic aspects of the TAC calculations within the self-consistent framework. Section III A briefly recalls previous studies on chiral rotation in the four $N = 75$ isotones considered here. Section III B describes all technical details of the present calculations, in particular the way in which the role of time-odd nucleonic densities was examined. Energy minima obtained for nonrotating states are listed in Sec. III C. In Sec. III D, rotational properties of the valence nucleons and of the core are examined within standard principal-axis cranking (PAC). In Sec. III E we solve a simple classical model of chiral rotation and show that such a rotation cannot exist below a certain critical angular frequency. The HF solutions for planar and chiral rotation are presented in Secs. III F and III G, respectively. In Sec. III H we demonstrate that our results obtained for the three-dimensional rotation can actually be represented as a sum of three independent one-dimensional rotations about the principal axes. The values obtained for the critical frequency and the agreement of our results with experimental level energies are discussed in Sec. IV. In the appendix we study response of the s.p. angular momenta to three-dimensional rotation, and we introduce the notions of *soft* and *stiff* alignments.

II. HARTREE-FOCK TILTED-AXIS-CRANKING CALCULATIONS

So far, the TAC model has been described in the literature only in its PQTAC and SCTAC variants [15–17]. Therefore, in this section we give several details that are specific for its self-consistent implementation. The discussion concerns mainly the way of iteratively solving the HF equations adopted in this work.

As far as nonrotating states are concerned, the HF method consists in minimizing the expectation value of the many-body Hamiltonian $\hat{H} = \hat{T} + \hat{V}$ in the trial class of Slater determinants. Here, $\hat{T}$ is the kinetic-energy operator, and

$\hat{V}$ is a two-body effective interaction. Equivalently, one can formulate the method in terms of the energy density functional $E\{\rho\}$, which is minimized with respect to the one-body density matrix ρ on which it depends, and this latter representation is used in the present study. Since $\hat{H}$ or the density functional $E\{\rho\}$ are invariant under rotations in space, it is clear that the HF solution is defined only up to an arbitrary rotation. For each solution it is useful to introduce an intrinsic frame of reference, whose axes we define as principal axes of the tensor of the electric quadrupole moment of the mass distribution. Because of this arbitrariness, this frame can be rotated with respect to the frame originally used to solve the HF equations, which we refer to as the program (or computer-code) frame. The program frame is the one defined by the axes x, y or z used for solving the mean-field equations (e.g., in a computer code).[1]

To describe rotational excitations within the TAC approach, in the program frame one imposes a linear constraint on angular momentum and minimizes the expectation value of the Routhian,

$$\hat{H}' = \hat{H} - \boldsymbol{\omega} \cdot \hat{\boldsymbol{I}}, \tag{1}$$

or the energy density in the rotating frame,

$$E'\{\rho\} = E\{\rho\} - \boldsymbol{\omega} \cdot \mathrm{Tr}(\hat{\boldsymbol{I}}\rho), \tag{2}$$

where $\hat{\boldsymbol{I}}$ is the total angular momentum operator, and vector $\boldsymbol{\omega}$, the rotational frequency vector, is composed of three Lagrange multipliers. Its components in the program frame are fixed as part of the definition of $\hat{H}'$ or $E'\{\rho\}$. Because of the rotational invariance, solutions obtained for the same length, but different directions of $\boldsymbol{\omega}$, differ only by their orientation in the program frame, so that only the length $\omega = |\boldsymbol{\omega}|$ has physical meaning.

Within the HF procedure, one obtains that the sought Slater determinant or the one-body density is built of the eigenstates of the s.p. Routhian,

$$\hat{h}' = \hat{h} - \boldsymbol{\omega} \cdot \hat{\boldsymbol{I}}, \tag{3}$$

where the mean-field Hamiltonian $\hat{h} = \hat{T} + \hat{\Gamma} = \delta E\{\rho\}/\delta\rho$ is a sum of the kinetic energy $\hat{T}$ and the mean field $\hat{\Gamma}$. A non-self-consistent approximation to the HF method consists in replacing $\hat{\Gamma}$ with a model potential, whose deformation dependence is usually parametrized in terms of the multipole deformations of the nuclear surface. Then, the expectation value of the Routhian, $\hat{h}'$, is minimized over the deformation parameters of the potential, which allows us to achieve self-consistency with respect to the nuclear shape.

In the PQTAC/SCTAC implementations of this approach, a hybrid [26] of the Woods-Saxon [33] and Nilsson [34] s.p. potentials is taken. The quadrupole-quadrupole interaction of PQTAC just amounts to the deformation, whereas SCTAC takes into account the nuclear liquid-drop energy within the standard Strutinsky method [35,36].

---

[1]It would be unfortunate to call it the laboratory frame, because in the common interpretation of the cranking model, both the program and the intrinsic frames rotate in the laboratory system. However, the program and intrinsic frames do not move with respect to each other—they differ only by the orientation of their axes.

Obviously, only the relative orientation of the angular momentum vector with respect to the nuclear body carries physical information. Common orientation of the angular momentum vector and nucleonic densities with respect to the program frame can thus be arbitrary. In the PQTAC/SCTAC method, where the orientation in space of the nuclear surface is under control via the multipole deformations $\alpha_{\lambda\mu}$, one can take advantage of this fact and fix $\alpha_{21} = \text{Im } \alpha_{22} = 0$ so that the intrinsic and program frames coincide. Minimization of the expectation value of the Routhian, $\hat{h}'$, at a given magnitude of ω is then performed by varying the direction of ω and all $\alpha_{\lambda\mu}$ except of α_{21} and $\text{Im } \alpha_{22}$.

In the HF method, however, the Euler angles defining the orientation of the intrinsic axes in the program frame are not free variational parameters, but complicated functions of densities, which in turn change from one HF iteration to another. The only possible way to make the two frames coincide is by imposing dynamical constraints on the off-diagonal components of the quadrupole tensor and requiring that they vanish. Then, one can vary the cranking-frequency vector as in the PQTAC/SCTAC approach. This is actually the only way to proceed if the energy dependence on the intrinsic orientation of ω is sought. However, constraints strong enough to confine the nucleus easily lead to divergences, and adjusting their strengths properly may be a cumbersome task. If only the energy minimum is of interest, a more natural and incomparably faster way is to fix ω in the program frame and let the mean potential reorient and conform to it self-consistently in the course of the iterations. The intrinsic axes now do become tilted with respect to the program frame.

The Kerman-Onishi theorem [37] states that in each self-consistent solution the total angular momentum vector $\mathbf{I} = \langle \hat{\mathbf{I}} \rangle$ is parallel to ω. In calculations, the angle between those vectors converges to zero very slowly in terms of the HF iterations, because the whole nucleus must turn in the program frame to align its $\mathbf{I}$ with the fixed ω. Therefore, a much faster procedure is to explicitly reset ω in each iteration to make it parallel to the current $\mathbf{I}$, while keeping its length ω constant [30]. This purely heuristic procedure does not correspond to a minimization of any given Routhian. However, once the self-consistent solution is found, it is the Routhian for the final angular frequency that takes its minimum value.

Some quantities, such as mean angular momenta and multipole moments, are easiest to discuss only when expressed in the intrinsic frame of the nucleus, but it is a natural way to calculate them first in the program frame. Since the two frames do not necessarily coincide, one has to find the axes of the intrinsic frame by diagonalization of the quadrupole deformation tensor and to transform the considered quantities into that frame by use of the Wigner matrices. (Such a procedure may fail when the solutions have vanishing quadrupole moments, but in the present paper such cases are of no interest and will not be discussed.)

The HF TAC solutions are arbitrarily tilted with respect to the program frame moreover, their orientation is not known a priori. Therefore, when solving the problem numerically one should ensure such conditions that the same solution be represented equally well in all orientations. In particular, the energy must not depend on the orientation. If the s.p.

wave functions are expanded onto a basis, this means that the choice of the s.p. basis and of the basis cutoff must not privilege any axis of the reference frame. In the case of the Cartesian harmonic-oscillator (HO) basis used in the present study, this by definition amounts to taking the three oscillator frequencies equal and including only the entire HO shells. To obtain a reasonable description of deformed nuclei in such nondeformed bases, the only way is to use sufficiently many HO shells.

III. RESULTS

A. Experiment and previous calculations

In the present study, the HF solutions corresponding to chiral rotation were sought in four $N = 75$ isotones, ^{130}Cs, ^{132}La, ^{134}Pr, and ^{136}Pm. These are the first nuclei in which candidate chiral bands were observed and systematically studied [2]. For the most recent experimental data refer to [10] for ^{130}Cs, to [9,12,38] for ^{132}La, to [2,39] for ^{134}Pr, and to [40] for ^{136}Pm. Absolute values of spins and reduced transition probabilities were measured only in ^{132}La. The possible chiral bands known in this nucleus are shown in Fig. 1 with full symbols. The lowest one (circles) is the yrast in positive parity. Two closely lying excited bands, B1 and B3 (squares and diamonds), are known [7–9], and it is unclear which one should be viewed as the chiral partner of the yrast band. The yrast and B1 bands are of positive parity with known spins, but for band B3 the spin assignments are tentative.

For all the $N = 75$ isotones in question, PRM calculations were performed [11,12,40,41], and generally a good agreement with experiment could be obtained for both the energies and the $B(M1)/B(E2)$ ratios, with a proper adjustment of the model parameters. Lifetime measurements in ^{132}La [7–9] revealed, however, that absolute values of the reduced transition probabilities significantly deviate from these earlier PRM predictions.

PQTAC/SCTAC calculations with pairing were carried out for all the considered nuclei as well [2,20,24], and these are also quoted in Refs. [21–23]. Quadrupole deformations ϵ of $0.16, 0.175, 0.175$, and 0.195 and triaxialities $\gamma \approx 39°, 32°, 27°$, and $26°$ were found, respectively, for ^{130}Cs, ^{132}La, ^{134}Pr, and ^{136}Pm. Chiral solutions were obtained in a limited range of angular frequency. The lower limits corresponded to the critical frequency ω_{crit} discussed in the present work. Only Refs. [20] and [24] quote their values, which are $\omega_{\text{crit}} = 0.3 \text{ MeV}/\hbar$ for ^{134}Pr and $\omega_{\text{crit}} < 0.2 \text{ MeV}/\hbar$ for ^{136}Pm. Comparison with experimental energies was given only for ^{134}Pr in Refs. [2,20], where the behavior of the bands was reproduced, on the average.

B. Details of the calculations

The present study is limited to the simplest chiral s.p. configuration, $\pi h_{11/2}^1 \nu h_{11/2}^{-1}$, which has been assigned in the literature to the candidate chiral bands observed in the $N = 75$ isotones. To check whether the existence of the HF chiral solutions is not a particular feature of one Skyrme parameter
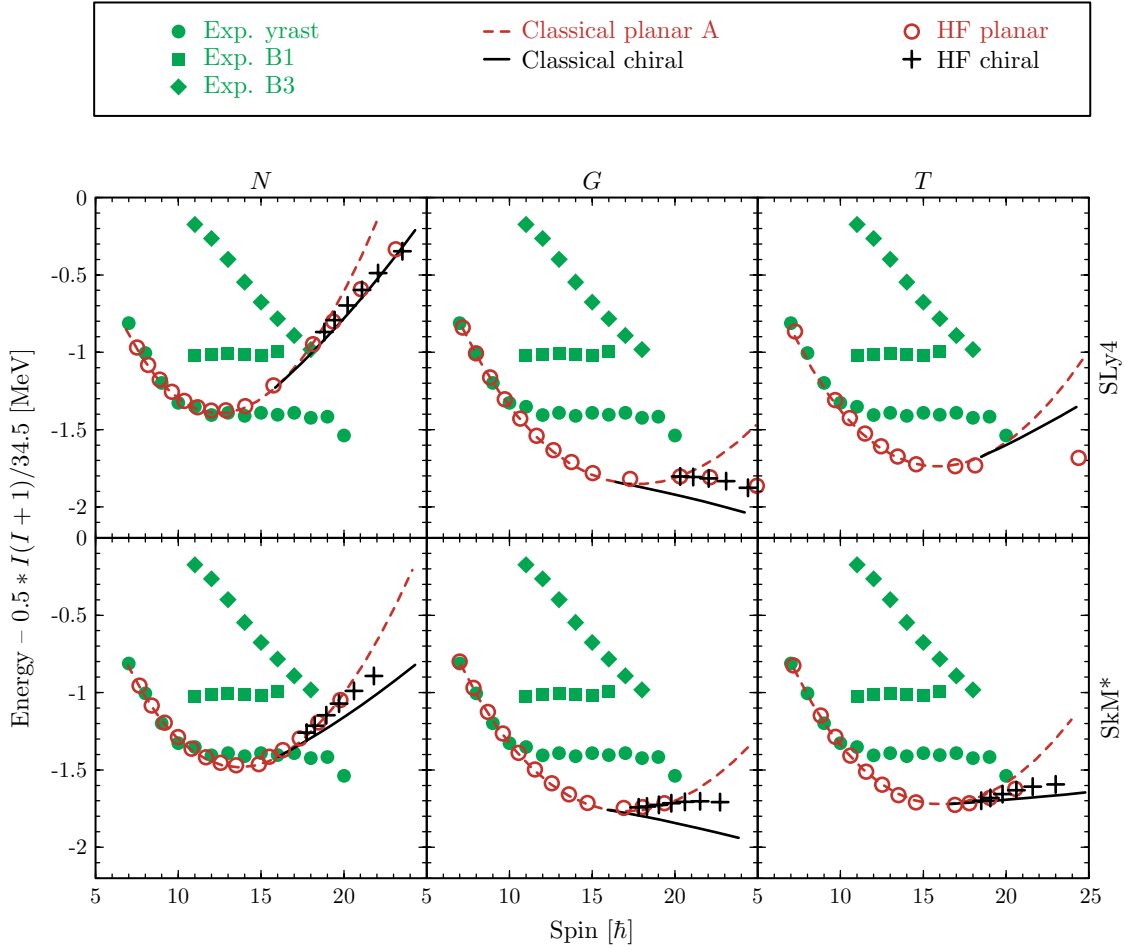
FIG. 1. (Color online). Energies obtained from the HF TAC calculations (open circles and plus symbols) and from the classical model presented in Sec. III D (dashed and solid lines) compared with the experimental data on the candidate chiral partner bands in ^{132}La (full symbols). The HF results obtained for the SLy4 and SkM* forces are shown for the N, G, and T time-odd fields included (see text).

set, all calculations were repeated with two parametrizations, SLy4 [27] and SkM* [28]. The parity was kept as a conserved symmetry, and the pairing correlations were not included.

In forming the chiral geometry, orientations of several angular momentum vectors play a crucial role. Their behavior depends on, among others, the nucleonic densities, which are odd under time reversal, such as the current and spin densities. Therefore, taking those densities and corresponding terms in the energy density functional into account seems important for the microscopic description of the chiral rotation. Self-consistent methods are best suited for such a task, and investigating the role of the time-odd densities was one of our priorities in the present study.

The Skyrme energy density functional depends on time-even and time-odd nucleonic densities with coupling constants C_t^ρ, $C_t^{\Delta\rho}$, C_t^τ, C_t^J, and $C_t^{\nabla J}$ (10 time-even terms) and with coupling constants C_t^s, $C_t^{\Delta s}$, C_t^T, C_t^j, and $C_t^{\nabla j}$ (10 time-odd terms) [42]. The index $t = 0, 1$ denotes the isoscalar and isovector parts. In standard parametrizations, which are used in the present work, C_t^ρ and C_t^s additionally depend on the isoscalar particle density. Under the assumption of local gauge invariance [42], there are several relations between the

time-even and time-odd coupling constants:

$$C_t^j = -C_t^\tau, \quad C_t^J = -C_t^T, \quad C_t^{\nabla j} = +C_t^{\nabla J}. \quad (4)$$

In the present calculations, the coupling constants C_t^J of the time-even terms for $t = 0, 1$ were always set to zero, as in the original fits of the forces SLy4 and SkM*. To conform to the local gauge invariance, whose consequence is Eq. (4), the coupling constants C_t^T of the time-odd terms were set to zero, too. Apart from C_t^J, all other time-even coupling constants were taken as they come from the parameters of the Skyrme force.

To examine the role of the time-odd densities, we have performed three variants of calculations, throughout the text denoted as N, G, and T, and defined in the following way:

(i) Variant N: All time-odd coupling constants are set to zero and the local gauge invariance conditions in Eq. (4) are violated.

(ii) Variant G: Coupling constants C_t^j and $C_t^{\nabla j}$ are taken as they come from the parameters of the Skyrme force and as required by the local gauge invariance (4); all other time-odd coupling constants are set to zero.

TABLE I. Quadrupole β and γ deformation parameters, parameters of the classical model, $\mathcal{J}_{s,m,l}$ [$\hbar^2$/MeV], $s_{s,l}$ [$\hbar$], classical estimates for the critical frequencies and spins, $\omega_{\text{crit}}^{\text{clas}}$ [MeV/$\hbar$] and $I_{\text{crit}}^{\text{clas}}$ [$\hbar$], and the full HF TAC results for those quantities, $\omega_{\text{crit}}^{\text{HF}}$ [MeV/$\hbar$] and $I_{\text{crit}}^{\text{HF}}$ [$\hbar$], for the $N = 75$ isotones. The HF results with the SLy4 and SkM* forces are shown for the N, G, and T variants of calculation defined in Sec. III B.

Nucleus	Force		β	γ	$\mathcal{J}_s$	$\mathcal{J}_m$	$\mathcal{J}_l$	s_s	s_l	$\omega_{\text{crit}}^{\text{clas}}$	$I_{\text{crit}}^{\text{clas}}$	$\omega_{\text{crit}}^{\text{HF}}$	$I_{\text{crit}}^{\text{HF}}$
^{130}Cs	SLy4	N	0.24	49	4.81	29.2	17.0	5.41	4.86	0.46	12.8		
		G	0.24	49	5.50	37.1	21.3	5.45	5.16	0.37	13.2		
		T	0.24	49	4.16	29.4	19.9	5.49	5.20	0.59	16.8		
	SkM*	N	0.23	47	5.86	31.3	17.9	5.43	5.01	0.43	13.0		
		G	0.23	47	6.55	36.7	21.1	5.47	4.97	0.37	13.0		
		T	0.23	47	5.69	33.4	20.0	5.49	5.14	0.43	13.9		
^{132}La	SLy4	N	0.26	46	7.18	28.7	19.1	5.44	4.90	0.57	15.9	0.68	18.8
		G	0.26	46	8.45	36.0	23.7	5.60	5.21	0.47	16.4	0.60	20.3
		T	0.26	46	7.12	31.7	22.2	5.64	5.26	0.60	18.5		
	SkM*	N	0.25	45	8.19	30.8	20.3	5.47	5.03	0.54	16.0	0.62	17.8
		G	0.25	45	8.81	35.9	23.5	5.60	5.06	0.46	15.9	0.54	17.8
		T	0.25	45	8.37	34.0	22.4	5.63	5.21	0.50	16.5	0.58	18.5
^{134}Pr	SLy4	N	0.26	58	6.11		25.4	5.00	4.36				
	oblate	G	0.26	58	7.21		31.3	4.92	4.84				
		T	0.26	56	3.68		29.8	5.26	4.60				
	SkM*	N	0.23	22	18.5	28.1	20.7	5.38	5.28	0.91	25.0		
	triaxial	G	0.23	22	21.4	32.6	24.3	5.46	5.44	0.82	26.1		
		T	0.23	22	20.7	30.8	24.8	5.52	5.57	1.08	32.7		
^{136}Pm	SLy4	N	0.25	53			24.7		4.62				
	oblate	G	0.25	53			30.3		5.38				
		T	0.25	52			29.0		5.05				
	SkM*	N	0.22	19	15.0	27.5	12.4	5.32	5.38	0.56	14.8		
	triaxial	G	0.22	19	17.9	33.2	13.0	5.50	5.42	0.45	14.4		
		T	0.22	19	17.4	29.8	13.4	5.51	5.53	0.56	16.1		

(iii) Variant T: Apart from C_t^T, all other time-odd coupling constants are taken as they come from the parameters of the Skyrme force and as required by the local gauge invariance (4).

Setting or not setting some time-odd coupling constants to zero implies excluding or including in the calculations the corresponding time-odd terms of the mean field. In variant N, the mean field contained only the time-even contributions (apart from the cranking term) as in the case of the non-self-consistent s.p. potentials.

The calculations were carried out by using the code HFODD (v2.05c) [29–31]. The code expands the s.p. wave functions onto the HO basis and uses the iterative method to solve the HF equations. Twelve entire spherical HO shells were included in the basis. It has been verified that increasing this number up to 16 changes the quantities important for the present considerations (deformation, moments of inertia, alignments, etc.) by less than 1%.

C. Energy minima in the $N = 75$ isotones

As the first step, the HF calculations without cranking were performed to find the $\pi h_{11/2}^1 \, \nu h_{11/2}^{-1}$ bandheads. Obviously,

the energetically most favored state of this configuration is obtained if the valence proton particle and neutron hole occupy the lowest and highest levels of the $h_{11/2}$ multiplets, respectively. Table I gives the obtained β and γ deformations for each isotone and Skyrme parameter set. They practically do not depend on the included time-odd terms, and they remain almost constant when cranking is applied later on in our calculations. Note that the present values of β are up to 1.5 times larger than those found in the PQTAC/SCTAC calculations quoted in Sec. III A. Also the values of γ are more distant from the maximum triaxiality of $30°$ compared to the earlier results by other authors.

In ^{134}Pr and ^{136}Pm, two minima with the same $\pi h_{11/2}^1 \, \nu h_{11/2}^{-1}$ configuration were found; these differ by the occupation of positive-parity states. The energetically lower minima have positive-parity s.p. structure similar to that in ^{130}Cs and ^{132}La, but they correspond to almost oblate shapes of $\gamma = 53°$–$58°$. The other minima have $\gamma = 19°$–$22°$, thus corresponding to triaxial shapes. In the following, those two kinds of minima in ^{134}Pr and ^{136}Pm are conventionally referred to as *oblate* and *triaxial*. Such a structure of minima and configurations appears for both interactions studied here, SkM* and SLy4, and the corresponding sets of results are very similar to one another. Therefore, to save space, in the following only the SkM* results

are shown for the *triaxial* minima and only the SLy4 results for the *oblate* ones.

In Sec. II, we introduced the intrinsic frame of a nucleus as formed by the principal axes of the quadrupole tensor. In the following, by the short (s), medium (m), and long (l) axes of our triaxial solutions we understand the intrinsic axes indexed so that $\langle x_s^2 \rangle < \langle x_m^2 \rangle < \langle x_l^2 \rangle$, where x_i is the Cartesian coordinate for axis $i = s, m$, or l.

D. Properties of the $h_{11/2}$ valence nucleons and of the core

We began our study of rotational properties by performing the standard PAC calculations, in which we examined rotations of the found triaxial HF solutions about their short, medium, and long axes. Let us recall that for the PAC about the principal axis $i = s, m, l$, not only the cranking-frequency vector $\boldsymbol{\omega}$ but all the resulting s.p. and total mean angular momentum vectors $\boldsymbol{j}$ and $\boldsymbol{I}$ have nonzero components ω_i, j_i, and I_i only on that axis.

Figure 2 gives the s.p. Routhians obtained from the PAC calculations in ^{132}La with the SLy4 force, without the time-odd fields. Routhians for other isotones, forces, and time-odd terms included do not differ in their main features from the ones shown. The upper and lower parts show the proton and neutron levels, respectively, and the left, middle, and right panels correspond to cranking about the short, medium, and long axes. Positive-parity and negative-parity levels are marked with solid and dashed lines. The negative-parity levels belonging to the $h_{11/2}$ multiplet are marked with crosses. The Routhians occupied by the valence $h_{11/2}$ proton particle and neutron hole are marked with full and open circles, respectively.

In both kinds of nucleons, the lowest levels of the $h_{11/2}$ multiplet split strongly for cranking about the short axis and have almost zero slope for the two remaining axes. The highest $h_{11/2}$ levels behave similarly, but they split in the case of the rotation about the long axis. The intermediate levels split for cranking about each axis, but only weakly.

For the PAC about the ith axis, slopes of the s.p. Routhians, e', approximately translate into the s.p. angular momentum alignments j_i on that axis according to the well-known formula

$$j_i \approx -\frac{de'}{d\omega_i}, \tag{5}$$

which holds almost exactly in the present case, because changes of the mean field with rotational frequency are negligible. Thus, one can infer from Fig. 2 that the valence $h_{11/2}$ proton particle and neutron hole have nonzero alignments j_i^p and j_i^h only for the PAC about short and long axes, respectively. This can be seen directly in Fig. 3, which shows j_i^p and j_i^h calculated as mean values of the angular momentum operator for the variant G of the calculations with the SLy4 force. Results for the short, medium, and long axes are plotted with dotted, solid, and dashed lines, respectively.

It turns out that further important properties of the valence $h_{11/2}$ particle and hole can be deduced from pure symmetry considerations, which we present in the appendix. We consider an isolated twofold degenerate s.p. level in a fixed potential symmetric with respect to the D_2 group (rotations by 180° about the three principal axes). The main conclusion relevant for the present case is the following. If in the PAC an s.p. state

has a nonzero alignment j_i only for rotation about one principal axis, then in the TAC its angular momentum vector $\boldsymbol{j}$ will point along that axis and remain approximately constant regardless of the length and direction of the applied cranking frequency $\boldsymbol{\omega}$. We call this a *stiff alignment*. Thus, the angular momenta $\boldsymbol{j}^p$ and $\boldsymbol{j}^h$ of the valence $h_{11/2}$ proton particle and neutron hole are stiffly aligned along the short and long intrinsic axes, respectively, as expected for the chiral geometry.

In our self-consistent calculations, the s.p. spectrum of the mean-field Hamiltonian $\hat{h}$ of Eq. (3) exhibits the twofold Kramers degeneracy only in variant N of the calculations, when no time-odd fields are taken. It seems that the lowest and highest $h_{11/2}$ levels can be indeed treated as isolated: Their angular momentum coupling to other s.p. states is weak, which can be seen from the small curvature of their PAC Routhians in Fig. 2. The assumption about fixed potential is also justified, because in our results the deformation remains nearly constant with rotational frequency.

In the present case, the remnant coupling to other states and changes of the mean field alter the ideal picture in that $\boldsymbol{j}^p$ and $\boldsymbol{j}^h$ are not strictly constant but show some remnant dependence on the cranking frequency. As illustrated in Fig. 3, this dependence is to an approximation linear, and the PAC alignments can be written in the form

$$\boldsymbol{j}^p \simeq s_s \boldsymbol{i}_s + \delta\mathcal{J}^p \boldsymbol{\omega}, \qquad \boldsymbol{j}^h \simeq s_l \boldsymbol{i}_l + \delta\mathcal{J}^h \boldsymbol{\omega}, \tag{6}$$

where $\boldsymbol{i}_s$ and $\boldsymbol{i}_l$ denote the unit vectors along the short and long axes, respectively. The quantities s_s and s_l are initial alignments at vanishing frequency, and $\delta\mathcal{J}^p$ and $\delta\mathcal{J}^h$ are tensor coefficients, representing the s.p. contributions to the total inertia tensor $\mathcal{J}$ of the nucleus.

The PAC allows us to estimate the diagonal components of $\delta\mathcal{J}$, which are slopes of the $j_i(\omega_i)$ curves plotted in Fig. 3. One can see from the figure that they can be as large as $\sim$4 $\hbar^2$/MeV. This is a significant value compared to the total moments of inertia, discussed in the following and collected in Table I. For ^{123}La, the total moments are of the order of $\sim$(8–36) $\hbar^2$/MeV, depending on the axis.

The same PAC calculations provide the total alignments I_s, I_m, and I_l on the short, medium, and long axes, respectively. They are plotted in Fig. 4 with dotted, solid, and dashed lines, correspondingly, for all the considered cases. In the nearly *oblate* minima in ^{134}Pr and ^{136}Pm, an attempt to crank around the medium axis leads to such a self-consistent readjustment of the shape that solutions corresponding to the rotation about the long axis are obtained.

The bends in the curves in Fig. 4, like the ones for I_s in ^{130}Cs, are caused by smooth crossings of the s.p. levels. Otherwise, the $I_i(\omega_i)$ dependence is linear to a good approximation, and therefore the rotation can be called rigid. The corresponding slopes give the collective total moments of inertia $\mathcal{J}_s$, $\mathcal{J}_m$, and $\mathcal{J}_l$ with respect to the short, medium, and long axes. They contain the valence particle and the valence hole contributions, $\delta\mathcal{J}^p$ and $\delta\mathcal{J}^h$, defined in Eq. (6).

At zero frequency, the cranking around the medium axis gives a vanishing angular momentum, whereas the cranking around the other two axes give nonzero limiting values, equal to the initial alignments s_s and s_l of the odd particle and hole. In view of the considerations presented later in this paper,
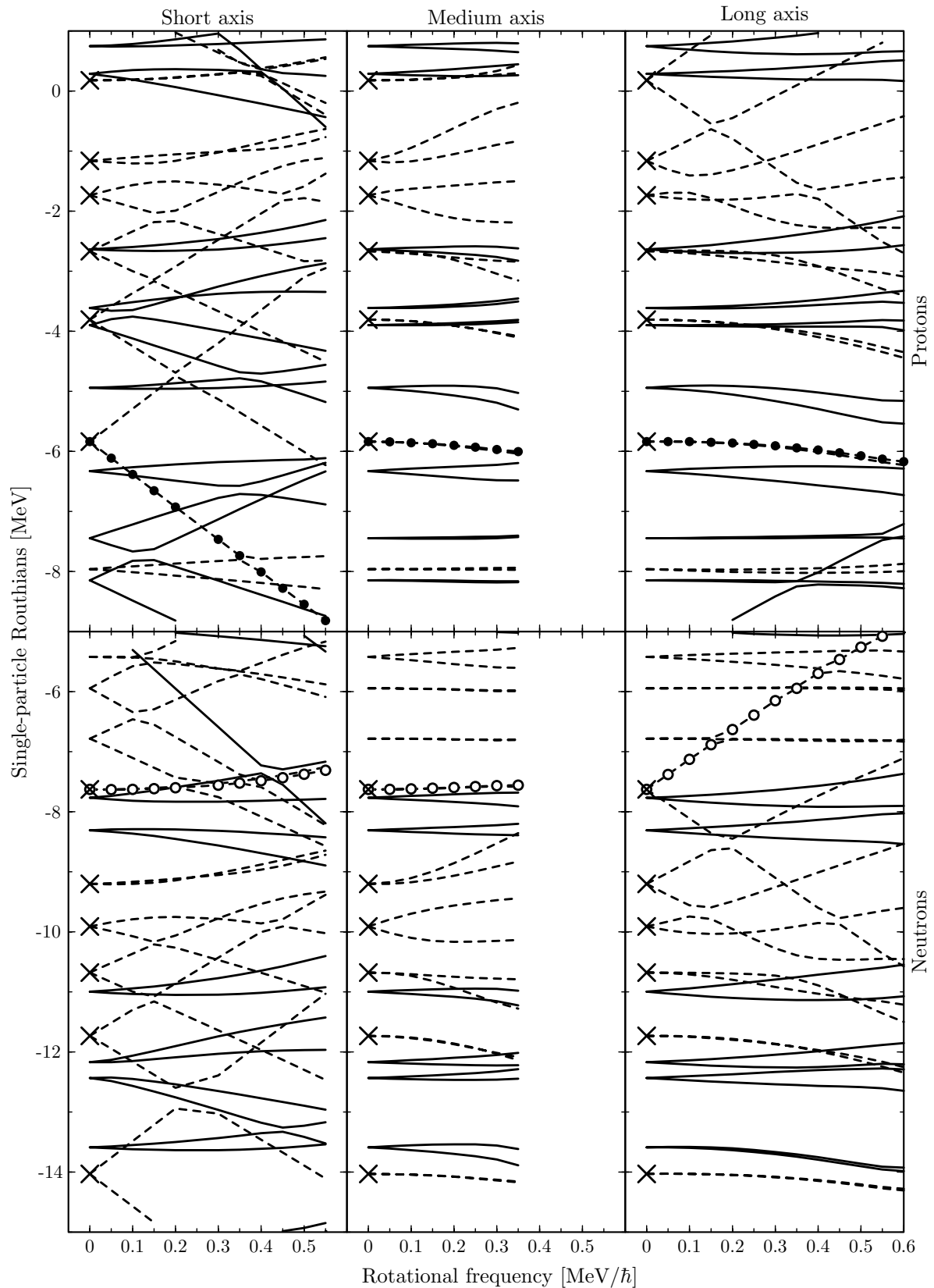
FIG. 2. Single-particle Routhians from the HF PAC calculations in ^{132}La with the SLy4 force and no time-odd fields. Proton (upper half) and neutron (lower half) Routhians for cranking about the short, medium, and long axes are shown. Positive-parity and negative-parity levels are marked with solid and dashed lines, respectively. Negative-parity levels belonging to the $h_{11/2}$ multiplet are marked with crosses. The Routhians occupied by the valence $h_{11/2}$ proton particle and neutron hole are marked with full and open circles, correspondingly.
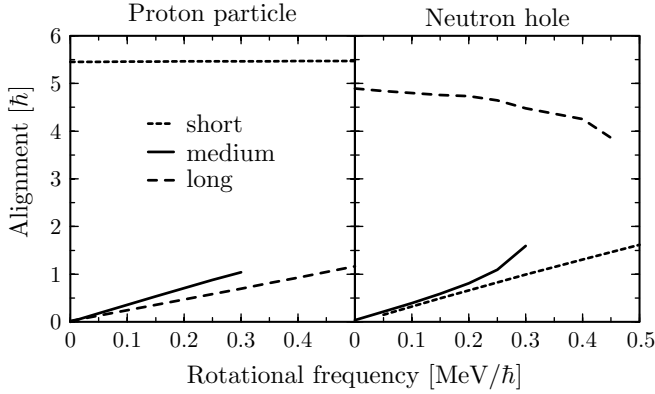
FIG. 3. Single-particle angular momentum alignments of the valence $h_{11/2}$ proton particle and neutron hole in ^{132}La, obtained from the PAC about the short, medium, and long axes. The HF results with the SLy4 force are shown for the G variant of calculation defined in Sec. III B.

we have extracted the actual values of the parameters $\mathcal{J}_s$, $\mathcal{J}_m$, $\mathcal{J}_l$, and s_s, s_l by fitting straight lines to the calculated alignment versus. frequency curves shown in Fig. 4. Whenever there was a bend in the calculated dependence, the line was fitted in the rotational frequency range below the bend. Since the alignment on the short axis for the *oblate* minimum in ^{136}Pm shows a particularly complicated behavior, we have not assigned any value to $\mathcal{J}_s$ in this case. The obtained values of the parameters are listed in Table I and are discussed in Sec. IV. These results confirm that the moment of inertia with respect to the medium axis is the largest.

The PAC method allows estimates of the diagonal components $\mathcal{J}_s$, $\mathcal{J}_m$, and $\mathcal{J}_l$ of the inertia tensor $\mathcal{J}$ to be made. To examine, as far as possible, the off-diagonal components we performed a kind of perturbative test within the TAC method. We applied to the nonrotating self-consistent solutions the cranking-frequency vector $\boldsymbol{\omega}$ in several directions, performed only one diagonalization of the resulting s.p. Routhian (3), and investigated the response of the mean angular momentum $\boldsymbol{I}$. It turned out that the off-diagonal components of $\mathcal{J}$ are negligibly small in all the considered isotones.

The microscopic results presented so far suggest that the considered system can be modeled by two gyroscopes of spins s_s and s_l rigidly fixed along the short and long axes of a triaxial rigid rotor characterized by the moments of inertia $\mathcal{J}_s$, $\mathcal{J}_m$, and $\mathcal{J}_l$, of which $\mathcal{J}_m$ is the largest. It is instructive to solve the associated problem of motion in the classical framework, which is done in the next section.

E. Classical model

The classical model of chiral rotation was briefly introduced in Ref. [32]; here we give its more detailed description and discussion. To define the model, we begin with elementary considerations related to the dynamics of rigid bodies. By a classical gyroscope we understand an axial-shape rigid body with moments of inertia $\mathcal{J}_\parallel$ and $\mathcal{J}_\perp$ with respect to the symmetry axis and an axis perpendicular to it, respectively. Such a body spins with fixed angular frequency Ω around its

symmetry axis; one can imagine that this motion is ensured by a motor and frequency regulator such that Ω is strictly constant in time.

Furthermore, let us imagine that the spinning body is rigidly mounted on another rigid body that has triaxial inertia tensor and three moments of inertia, $\mathcal{J}_s'$, $\mathcal{J}_m'$, and $\mathcal{J}_l'$, with respect to its short, medium, and long axis, respectively. Then, the angular frequency Ω is maintained fixed with respect to the triaxial body, irrespective of how the whole device moves, and the angular frequency vector $\boldsymbol{\Omega}$ has by definition three time-independent components, Ω_s, Ω_m, and Ω_l. To simplify our considerations let us assume that the axis of the gyroscope coincides with the short axis of the triaxial body; that is, $\Omega_s = \Omega$, $\Omega_m = 0$, and $\Omega_l = 0$. In this case the principal axes of the tensor of inertia of the whole device coincide with those of the triaxial body, and the three moments of inertia of the device read

$$\begin{aligned} \mathcal{J}_s &= \mathcal{J}_s' + \mathcal{J}_\parallel, \\ \mathcal{J}_m &= \mathcal{J}_m' + \mathcal{J}_\perp, \\ \mathcal{J}_l &= \mathcal{J}_l' + \mathcal{J}_\perp. \end{aligned} \tag{7}$$

We assume that the device rotates with the total angular frequency vector $\boldsymbol{\omega}$, which in the moving frame of the triaxial body has components ω_s, ω_m, and ω_l. In general, these components may vary with time, although later we study only such a motion of the device when they are time-independent. The kinetic energy of the device is the sum of that of the triaxial body and gyroscope,

$$T = T_{\text{triax}} + T_{\text{gyro}}, \tag{8}$$

where

$$T_{\text{triax}} = \tfrac{1}{2}\left(\mathcal{J}_s'\omega_s^2 + \mathcal{J}_m'\omega_m^2 + \mathcal{J}_l'\omega_l^2\right), \tag{9}$$

$$T_{\text{gyro}} = \tfrac{1}{2}\left(\mathcal{J}_\parallel(\omega_s + \Omega)^2 + \mathcal{J}_\perp\omega_m^2 + \mathcal{J}_\perp\omega_l^2\right); \tag{10}$$

hence

$$T = \tfrac{1}{2}\left(\mathcal{J}_s\omega_s^2 + \mathcal{J}_m\omega_m^2 + \mathcal{J}_l\omega_l^2\right) + \mathcal{J}_\parallel\Omega\omega_s + \tfrac{1}{2}\mathcal{J}_\parallel\Omega^2. \tag{11}$$

We see that the total kinetic energy is a sum of three terms. The first one represents the rotation of the entire device irrespective of the fact that it contains a spinning gyroscope; It depends only on the total moments of inertia. The second one represents the additional energy coming from the spinning gyroscope and depends on its time-independent spin $s_s = \mathcal{J}_\parallel\Omega$; the third one is a constant and can be dropped from further considerations.

It is obvious that if we add two other gyroscopes aligned with the medium and long axes and spinning with spins s_m and s_l, respectively, the second term can be simply written as a scalar product $\boldsymbol{\omega} \cdot \boldsymbol{s}$, where vector $\boldsymbol{s}$ has components s_s, s_m, and s_l. In this case, the total moment of inertia $\mathcal{J}$ will be a sum of contributions from the triaxial body and three gyroscopes. We note in passing that exactly the same result is obtained for a single *spherical* gyroscope, $\mathcal{J}_\parallel = \mathcal{J}_\perp$, tilted with respect to the principal axes of the triaxial body in such a way that it has spin components equal to s_s, s_m, and s_l.

The total angular momentum $\boldsymbol{I}$ of the system reads

$$\boldsymbol{I} = \mathcal{J}\boldsymbol{\omega} + \boldsymbol{s}, \tag{12}$$
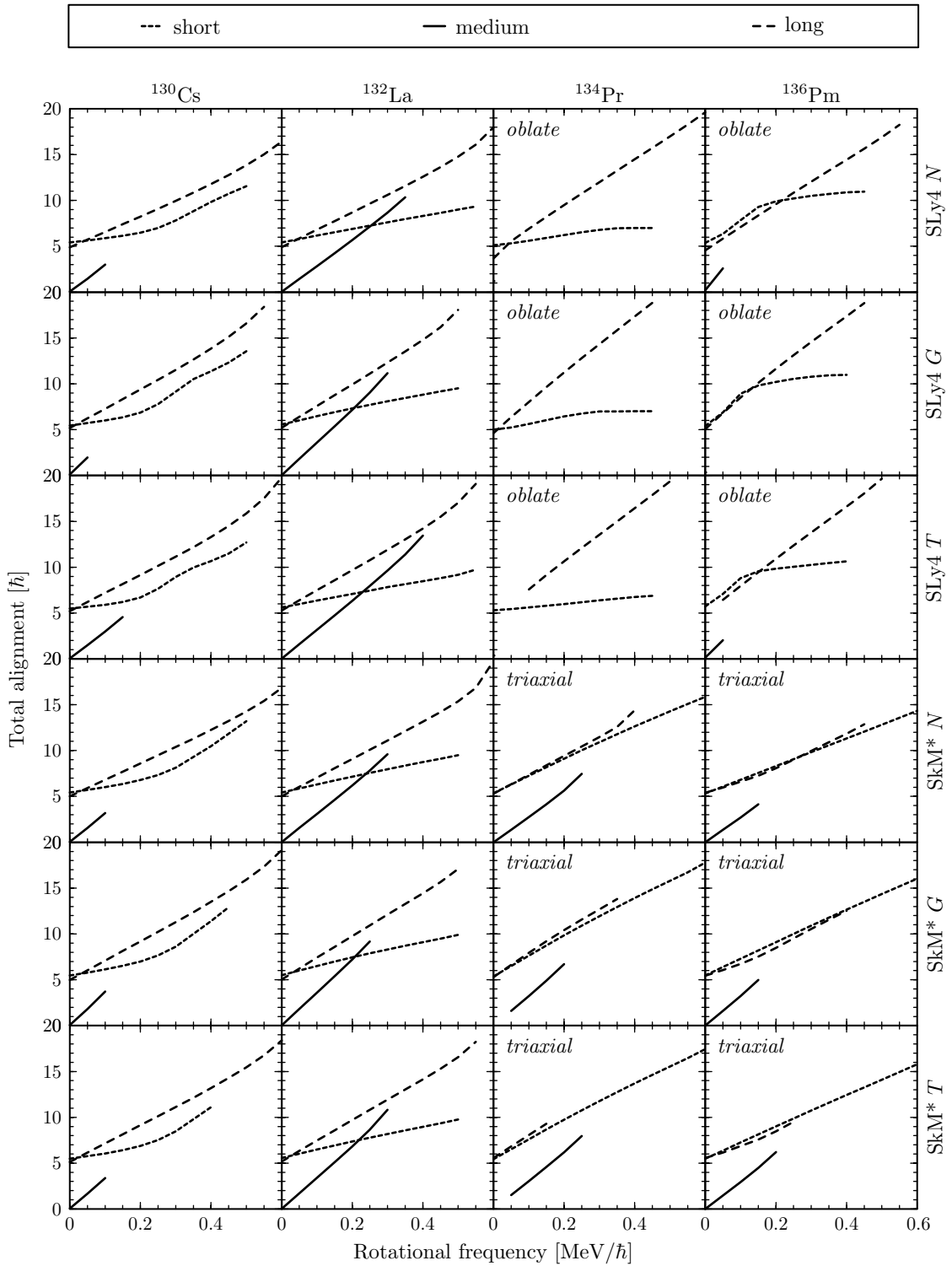
FIG. 4. Total angular momentum alignments obtained from the PAC about the short, medium, and long axes in ^{130}Cs, ^{132}La, ^{134}Pr, and ^{136}Pm. The HF results with the SLy4 and SkM* forces are shown for the N, G, and T variants of calculation defined in Sec. III B.

where s is the aforementioned vector sum of spins of all the gyroscopes and $\mathcal{J}\boldsymbol{\omega}$ stands for the tensor product of the moment of inertia tensor $\mathcal{J}$ with angular frequency vector $\boldsymbol{\omega}$. In the absence of potential interactions, the Lagrangian of the system is equal to the total kinetic energy (11), generalized to

the case of three gyroscopes, and thus is given by the formula

$$L = \tfrac{1}{2}\boldsymbol{\omega}\mathcal{J}\boldsymbol{\omega} + \boldsymbol{\omega} \cdot \boldsymbol{s}, \qquad (13)$$

where we dropped all constant terms. By taking the laboratory components of $\boldsymbol{\omega}$ as generalized velocities, it is easy to check

that the generalized momenta are equal to the laboratory components of I. This fact allows us to write the Legendre transformation [43] and to obtain the Hamiltonian of the system,

$$H = \boldsymbol{\omega} \cdot \boldsymbol{I} - L = \tfrac{1}{2}\boldsymbol{\omega}\mathcal{J}\boldsymbol{\omega}. \qquad (14)$$

Since the Lagrangian (13) does not depend explicitly on time, the Hamilton function (14) is a constant of motion and is identified with the total energy E of the system. Consider now a particular type of the Routhian [43], H', namely such that no variables undergo the Legendre transformation. In such a case, $H' = -L$, and by rewriting the Routhian in terms of the Hamiltonian one obtains

$$H' = H - \boldsymbol{\omega} \cdot \boldsymbol{I}. \qquad (15)$$

Equations of motion for the model can be derived in the following way. As for any vector, the time derivatives of the angular momentum vector ($\partial_t \boldsymbol{I}$, taken in the laboratory frame, and $\partial_t^\omega \boldsymbol{I}$, taken in a frame rotating with angular frequency $\boldsymbol{\omega}$) are related by the formula $\partial_t \boldsymbol{I} = \partial_t^\omega \boldsymbol{I} + \boldsymbol{\omega} \times \boldsymbol{I}$ [43]. Since the angular momentum is conserved in the laboratory frame, $\partial_t \boldsymbol{I} = 0$, one obtains the Euler equations [43] for the time evolution of the angular momentum vector in the body-fixed frame,

$$\partial_t^\omega \boldsymbol{I} = -\boldsymbol{\omega} \times \boldsymbol{I}. \qquad (16)$$

The mean-field cranking approximation can only account for the *uniform* rotations, in which the mean angular momentum vector is constant in the intrinsic frame of the nucleus: $\partial_t^\omega \boldsymbol{I} = 0$. Because of that, we restrict the classical model studied here to such uniform rotations. Because of Eq. (12), for uniform rotations also the angular frequency vector is constant in the intrinsic frame. The Euler equations (16) now take the form $\boldsymbol{\omega} \times \boldsymbol{I} = 0$ and require that $\boldsymbol{\omega}$ and $\boldsymbol{I}$ be parallel. The same condition holds for the HF solutions and is known as the Kerman-Onishi theorem; see Sec. II and Ref. [37]. The Euler equations can now be easily solved for the considered classical model. However, to show further analogies with the HF method, in what follows we find the uniform solutions by employing a variational principle.

According to Hamilton's principle, motion of a mechanical system can be found by making the action integral $\int L \, dt$ stationary. The real uniform rotations obviously belong to a wider class of trial motions with I and $\boldsymbol{\omega}$ being constant in the intrinsic frame, but not necessarily parallel to one another. Within this class, Lagrangian (13) does not depend on time. Therefore, extremizing the action for a given value of $\omega = |\boldsymbol{\omega}|$ reduces to finding extrema of the Lagrangian as a function of the intrinsic-frame components of $\boldsymbol{\omega}$. Since $H' = -L$, the Routhian (15) can be equally well used for this purpose. This provides us with a bridge between the classical model and the quantum cranking theory, where an analogous Routhian (1) is minimized in the space of the trial wave functions.

Extrema of H' with respect to the intrinsic-frame components of $\boldsymbol{\omega}$ at a given length of ω can be found by using a Lagrange multiplier $-\tfrac{1}{2}\mu$ for ω^2 (the factor $-1/2$ being added for later convenience). We continue further derivations for the case of two gyroscopes aligned along the s and l axes, as dictated by the microscopic results presented in Sec. III D;

that is, we employ the classical model for $s_m = 0$. Setting to zero the derivatives of the quantity

$$H' + \tfrac{1}{2}\mu\omega^2 = \tfrac{1}{2}\big[(\mu - \mathcal{J}_s)\omega_s^2 + (\mu - \mathcal{J}_m)\omega_m^2 + (\mu - \mathcal{J}_l)\omega_l^2\big] - (\omega_s s_s + \omega_l s_l) \qquad (17)$$

with respect to $\omega_s, \omega_m, \omega_l$, one obtains

$$\omega_s = s_s/(\mu - \mathcal{J}_s), \qquad (18)$$

$$\omega_m(\mu - \mathcal{J}_m) = 0, \qquad (19)$$

$$\omega_l = s_l/(\mu - \mathcal{J}_l). \qquad (20)$$

Equation (19) gives either $\omega_m = 0$ or $\mu = \mathcal{J}_m$, leading to two distinct classes of solutions.

If $\omega_m = 0$ then both $\boldsymbol{\omega}$ and $\boldsymbol{I}$ lie in the s-l plane. This gives planar solutions, for which the chiral symmetry is not broken. All values of μ are allowed, and the Lagrange multiplier must be determined from the length of $\boldsymbol{\omega}$ calculated in the obvious way from Eqs. (18) and (20). Figure 5(a) shows ω versus μ for sample model parameters, extracted from the ^{132}La HF PAC solutions with the SLy4 force with no time-odd fields, and listed in Table I. The solutions marked as A and D exist for all values of ω, whereas above some threshold frequency ω_{thr}, two more solutions appear, B and C. This threshold frequency can be determined by finding the minimum of ω as a function of μ and reads

$$\omega_{\text{thr}} = \frac{\big(s_s^{2/3} + s_l^{2/3}\big)^{3/2}}{|\mathcal{J}_l - \mathcal{J}_s|}. \qquad (21)$$

The value of ω_{thr} coming from the present HF calculations is rather high, higher than $1 \, \text{MeV}/\hbar$. Since bands B and C are situated far above the yrast line [see Fig. 5(d)] they will not be subject to further analysis.

For $\mu = \mathcal{J}_m$, all values of ω_m are allowed, whereas components in the s-l plane are fixed at $\omega_s = s_s/(\mathcal{J}_m - \mathcal{J}_s)$ and $\omega_l = s_l/(\mathcal{J}_m - \mathcal{J}_l)$. Consequently, the angular momentum has nonzero components along all three axes, and the chiral symmetry is broken. For each value of ω, there are two cases differing by the sign of ω_m, and thus giving the chiral doublet. The fact that ω_s and ω_l are constant leads to the principal conclusion that chiral solutions cannot exist for ω smaller than the critical frequency

$$\omega_{\text{crit}}^{\text{clas}} = \left[\left(\frac{s_s}{\mathcal{J}_m - \mathcal{J}_s}\right)^2 + \left(\frac{s_l}{\mathcal{J}_m - \mathcal{J}_l}\right)^2\right]^{1/2}. \qquad (22)$$

At that frequency, and with $\omega_m = 0$, the chiral solution coincides with the planar band A.

In $\boldsymbol{\omega}$ space, the four planar solutions form a hyperbola in the s-l plane, whereas the chiral doublet corresponds to a straight line perpendicular to that plane. These curves are shown in Fig. 5(b). Figure 5(c) gives the angular momentum as a function of rotational frequency for all the presented bands. With increasing ω, the so-called dynamical moment $\mathcal{J}^{(2)} \equiv dI/d\omega$ asymptotically approaches $\mathcal{J}_l$ for bands A and B and approaches $\mathcal{J}_s$ for bands C and D. For the chiral band, I is exactly proportional to ω with the coefficient $\mathcal{J}_m$. Thus, the critical spin $I_{\text{crit}}^{\text{clas}}$ corresponding to the critical frequency (22)
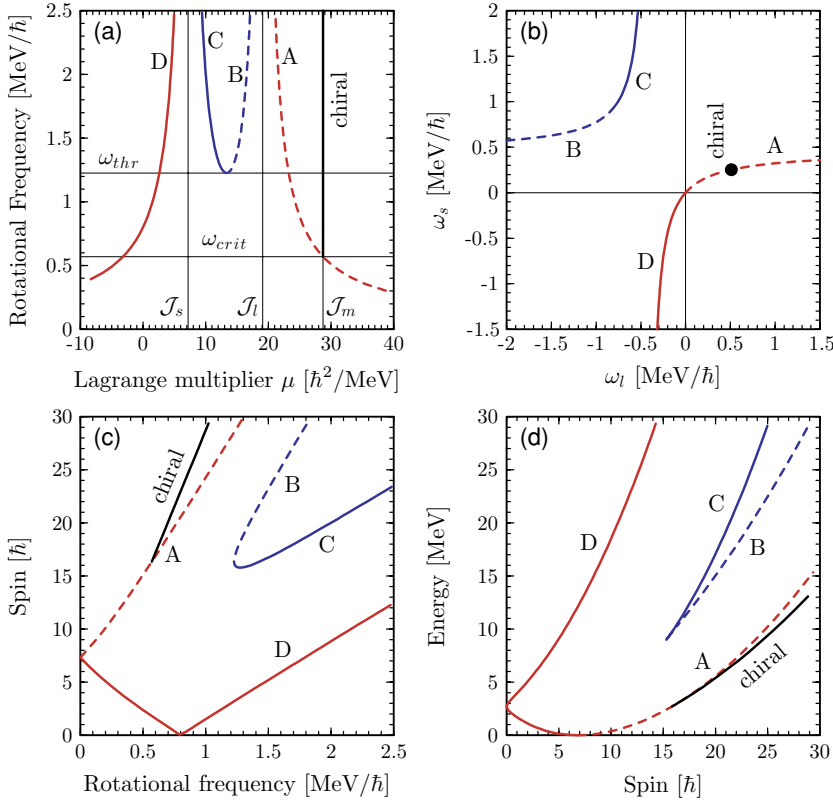
FIG. 5. (Color online) Planar bands A, B, C, and D and the chiral band obtained from the classical model. (a) Rotational frequency $\omega(\mu)$. (b) Intrinsic-frame trajectory of the rotational frequency vector $\boldsymbol{\omega}$. The chiral solution corresponds to a straight line perpendicular to the figure plane and intersecting it at the marked point. That perpendicular direction represents ω_m. (c) Angular momentum $I(\omega)$. (d) Energy $E(I)$.

reads

$$I_{\text{crit}}^{\text{clas}} = \mathcal{J}_m \omega_{\text{crit}}^{\text{clas}}. \tag{23}$$

Figure 5(d) summarizes the energies as a function of spin. The spin quantum number I is related to the length $|\boldsymbol{I}|$ of the angular momentum vector $\boldsymbol{I}$ by the condition $I(I+1) = |\boldsymbol{I}|^2$. At low angular momenta, the yrast line coincides with the planar band D. Then it continues along the planar solution A. Since the moment of inertia $\mathcal{J}_m$ is the largest, beyond the critical frequency the chiral solution becomes yrast, thereby yielding good prospects for experimental observation.

Altogether, the classical model described here is defined by five parameters, $\mathcal{J}_s$, $\mathcal{J}_m$, $\mathcal{J}_l$, s_s, and s_l, which are extracted form the microscopic HF PAC calculations and listed in Table I. The model can then be applied to predict properties of the planar and chiral TAC bands, and these predictions can be compared with the HF TAC results. Such a comparison is presented and discussed in the following sections.

F. Planar solutions

We began our self-consistent TAC calculations by finding planar solutions corresponding to the classical band A. The first point of each band of this kind was obtained by restarting the HF iterations from the previously converged nonrotating solution and by applying the initial cranking-frequency vector with nonzero components on its short and long intrinsic axes. Once convergence was achieved, the obtained solution served in turn as the starting point for the next value of the rotational frequency. We proceeded in this way with a frequency step

of 0.05 MeV/$\hbar$. We followed each band diabatically, that is, by exciting particles near the Fermi level whenever an empty and an occupied s.p. level of the same parity were about to cross, so that the states with the same physical properties were always occupied.

In the solutions corresponding to a planar rotation, the cranking-frequency vector had nonzero components on the short and long intrinsic axes in the self-consistent results. To give some insight into the s.p. structure of those solutions, in Fig. 6 we give the proton and neutron s.p. Routhians for the planar band in ^{132}La obtained with the SkM* force and no time-odd fields. Parts of the plots to the left of the thin vertical lines are relevant for the planar results. In contrast to the PAC Routhians of Fig. 2, now both the lowest and the highest $h_{11/2}$ levels split with rotational frequency. This is consistent with the picture that the valence particle and hole angular momenta $\boldsymbol{j}^p$ and $\boldsymbol{j}^h$, aligned on the short and long axes, respectively, now both have nonzero projections on the tilted axis of rotation.

To examine the angular momenta of the valence nucleons, $\boldsymbol{j}^p$ and $\boldsymbol{j}^h$, in Fig. 7 we plot their projections onto the short (dotted line), medium (solid line), and long (dashed line) intrinsic axes, for all the self-consistent solutions in ^{132}La. The positive and negative alignments are those of the lowest proton and highest neutron $h_{11/2}$ levels; the latter can be considered as representing $-\boldsymbol{j}^h$. Parts of the plots to the left of the thin vertical lines concern the planar bands. It can be seen that, indeed, the proton particle and the neutron hole align their angular momenta on the short and long axes. Furthermore, those alignments change rather weakly with rotational frequency, which means that the wave functions are strongly confined by deformation (deformation alignment).
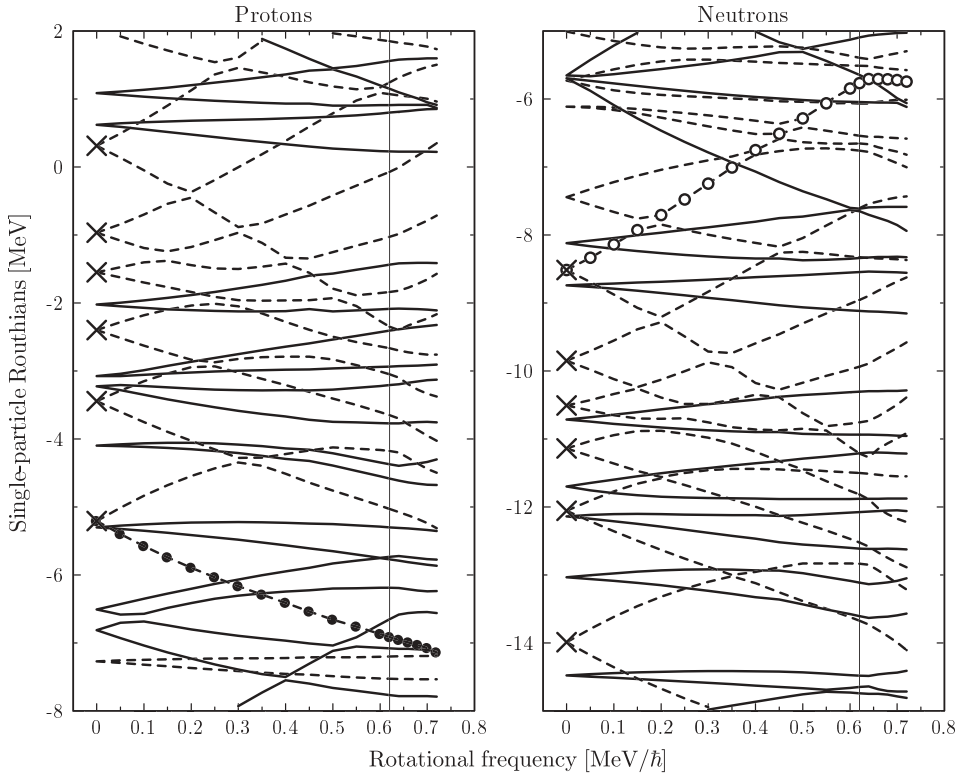
FIG. 6. Similar to Fig. 2 but for the proton and neutron s.p. Routhians from the HF TAC calculations with the SkM* force. The thin vertical line is drawn at $\omega_{\text{crit}}^{\text{HF}}$. The Routhians to the left and to the right of this line correspond to the planar and chiral bands, respectively.
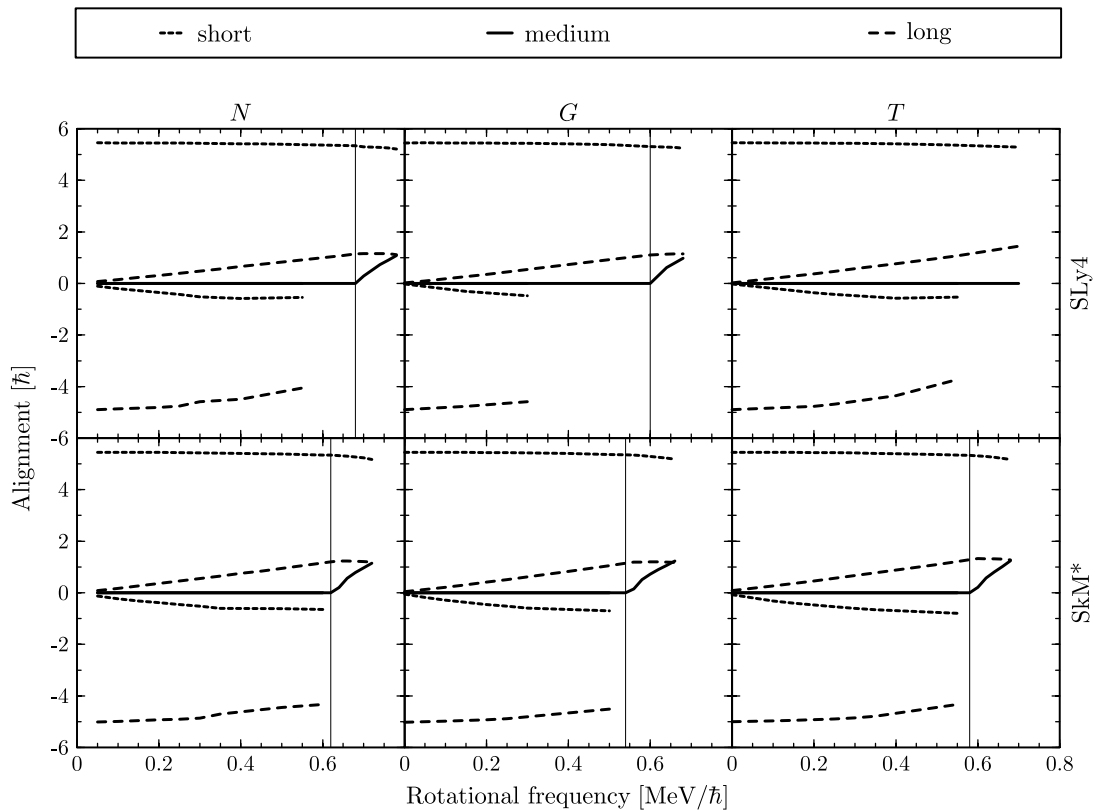

FIG. 7. Angular momentum alignments of the lowest proton (positive values) and highest neutron (negative values) $h_{11/2}$ levels on the short, medium, and long intrinsic axes from the HF TAC calculations in ^{132}La. The thin vertical line is drawn at $\omega_{\text{crit}}^{\text{HF}}$. The curves to the left and to the right of this line correspond to the planar and chiral bands, respectively. The HF results with the SLy4 and SkM* forces are shown for the N, G, and T variants of calculation defined in Sec. III B.
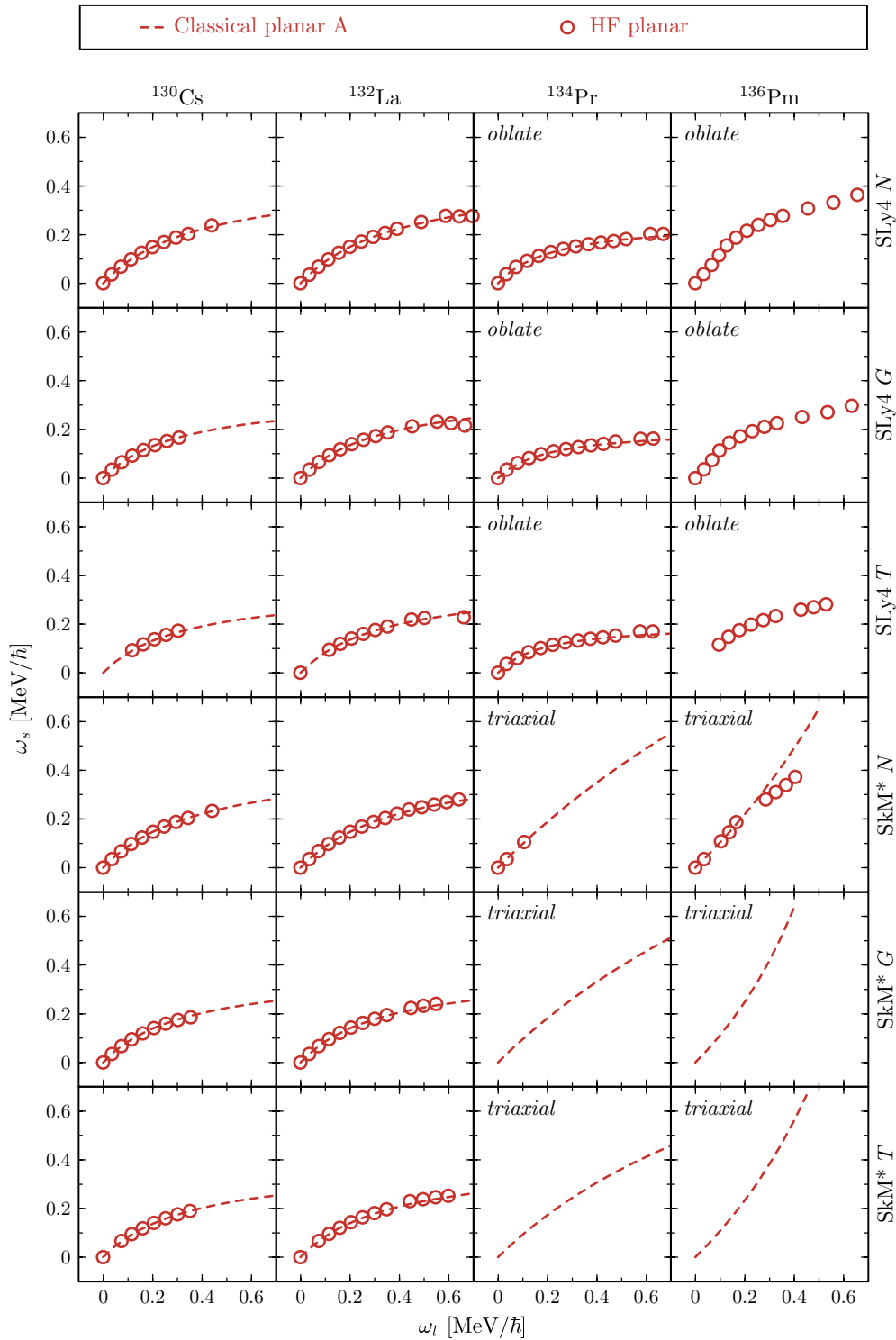
FIG. 8. (Color online) Intrinsic-frame trajectories of the angular frequency vector along the HF planar bands in the $N = 75$ isotones, compared to the classical solutions. The HF results with the SLy4 and SkM* forces are shown for the N, G, and T variants of calculation defined in Sec. III B.

It is worth emphasizing that the intrinsic-frame trajectories of ω along the self-consistent bands almost exactly follow the classical ones in all the considered cases. This is illustrated in Fig. 8, where the dashed lines represent classical A bands with parameters of Table I, and the HF results are marked

with open circles. For the *oblate* bands in ^{136}Pm the classical line is not shown because the parameters $\mathcal{J}_s$ and s_s could not be unambiguously extracted from the PAC calculations; see Sec. III D. However, the HF results follow a curve that very much resembles the classical hyperbola. For the *triaxial*

minima in ^{134}Pr and ^{136}Pm, no self-consistent planar bands could be obtained because of multiple level crossings.

Energy as a function of spin also shows a striking agreement between the classical and self-consistent results for the planar bands. This can be traced in the case of ^{132}La in Fig. 1 by following the same symbols as those in Fig. 8. Some deviations are visible only for rather high angular momenta.

G. Chiral solutions

The planar HF solutions were easily obtained by applying small cranking-frequency increments to the nonrotating state. For chiral bands, an analogous task was more difficult, because these bands start at finite frequencies, which in the present case are not lower than ≈ 0.5 MeV/$\hbar$. Several level crossings may occur between $\omega = 0$ and such a high frequency, and it is difficult to spot the required s.p. configuration at high frequencies. A hint on how to follow the $\pi h_{11/2}^1 \nu h_{11/2}^{-1}$ configuration diabatically comes from the classical prediction that the chiral band branches off from the planar solution (at the point corresponding to the critical frequency). One can thus restart iterations from the planar band by applying a cranking frequency with nonzero component on the medium axis.

As the first step we performed a kind of perturbative search along the planar bands, which turned out to be a very reliable test of where the chiral solution may exist. Such a search also gives us some understanding of why the chiral solutions do not appear in several cases. The procedure we applied was the following. To each converged point of the planar band, a small additional component ω_m of the angular frequency along the medium axis was added, with ω_s and ω_l unchanged. The resulting s.p. Routhian (3) was diagonalized only once. Then, it

was checked whether in the resulting non-self-consistent state the angular momentum and rotational frequency vectors were parallel, as required by the Kerman-Onishi necessary condition of self-consistency; see Sec. II. We can guess that in nuclei stiff against deformation changes, the direction of $\boldsymbol{I}$ is the only degree of freedom, and thus the Kerman-Onishi condition is also sufficient. If $\boldsymbol{I}$ is parallel to $\boldsymbol{\omega}$ in the non-self-consistent state after one diagonalization, then it is very probable that further iterations may lead to a converged chiral solution. Indeed, this was always the case, and no chiral solutions were obtained, in spite of several attempts, if that simple test gave a negative result.

The condition for $\boldsymbol{I}$ and $\boldsymbol{\omega}$ being parallel can be written in the form

$$\frac{I_s}{\omega_s} = \frac{I_m}{\omega_m} = \frac{I_l}{\omega_l}. \tag{24}$$

Note that the I_s/ω_s and I_l/ω_l ratios must be very close to each other in the non-self-consistent state, because the Kerman-Onishi condition is fulfilled for the self-consistent planar state. Therefore, the test consists in checking for each point of the planar band if I_m/ω_m is equal to $I_s/\omega_s \approx I_l/\omega_l$. In fact, this is reliable only if the time-odd fields are switched off, because in their presence, the I_m/ω_m ratio calculated perturbatively is significantly smaller than the self-consistent result would be. The reason is that the relevant components of the time-odd fields become active only after self-consistency is achieved for a nonzero ω_m. The test was made with $\omega_m = 0.05$ MeV/$\hbar$. These ratios, calculated for all the HF planar bands found in the $N = 75$ isotones, are plotted in Fig. 9. Plus symbols and open circles denote the HF values of I_m/ω_m and $I_s/\omega_s \approx I_l/\omega_l$,
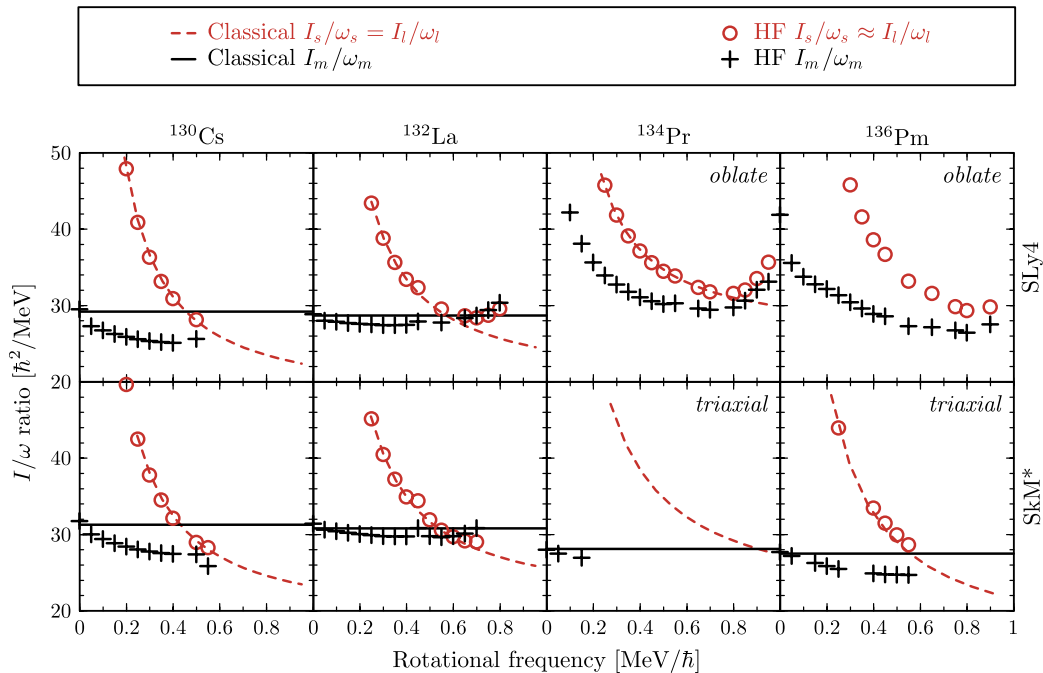

FIG. 9. (Color online) Ratios I_m/ω_m (plus symbols) and $I_s/\omega_s \approx I_l/\omega_l$ (open circles) obtained in the perturbative search for the HF chiral solutions along the planar bands in the $N = 75$ isotones; see text. Results for the SLy4 and SkM* forces with no time-odd fields are shown. Ratios I_m/ω_m (solid line) and $I_s/\omega_s = I_l/\omega_l$ (dashed line) corresponding to the classical-model chiral and planar bands, respectively, are also plotted for comparison.

respectively. To guide the eye, in the same figure we also plotted the ratios I_m/ω_m and $I_s/\omega_s = I_l/\omega_l$ corresponding to the classical-model chiral and planar bands, respectively.

It can be a priori expected that chiral solutions do not appear in the *oblate* minima in ^{134}Pr and ^{136}Pm, because of insufficient triaxiality. Indeed, the calculated values of the I_m/ω_m and $I_s/\omega_s \approx I_l/\omega_l$ ratios exhibit a complicated behavior and do not become equal to one another at any point. In ^{130}Cs, as well as in the *triaxial* minimum in ^{136}Pm, the two ratios clearly approach each other. It seems that the only reason why they do not attain equality is that the planar bands were not found up to sufficiently high frequencies, because of level crossings. Note, however, that the moment of inertia associated with the medium axis, I_m/ω_m, significantly drops with angular frequency, which takes I_m/ω_m away from $I_s/\omega_s \approx I_l/\omega_l$ and defers their equalization to higher frequencies. This effect is much weaker in ^{132}La, where the ratios do become equal, slightly above the point expected from the classical model. Indeed, self-consistent chiral solutions were found in this case, as described in the following.

After the first diagonalization of the perturbative test, the HF iterations were continued in each case to achieve self-consistency. In ^{130}Cs, ^{134}Pr, and ^{136}Pm, as well as for low rotational frequencies in ^{132}La, the iterations converged back to planar solutions. The same result was obtained for different initial orientations of $\boldsymbol{\omega}$ with respect to the intrinsic frame. This provides a strong argument that, for the concerned

configuration, no self-consistent chiral solutions exist at low frequencies. In ^{132}La, for ω high enough, converged solutions were obtained with $\boldsymbol{I}$ having nonzero components on all the three intrinsic axes, which corresponds to chiral rotation. To examine the chiral solutions independently of the planar ones, the fragments of chiral bands found were used as starting points to obtain solutions for lower and higher frequencies. Calculations were performed with an ω step of $0.02\,\text{MeV}/\hbar$. At a certain value of decreasing ω, the planar orientation of $\boldsymbol{I}$ was regained in the intrinsic frame, and the solution merged into the previously found planar one. In a natural way, that junction value of ω can be regarded as the Skyrme-HF result for the critical frequency and is denoted in the following as $\omega_{\text{crit}}^{\text{HF}}$. Values of $\omega_{\text{crit}}^{\text{HF}}$ obtained in the present calculations are collected in Table I and are discussed in Sec. IV. On the side of highest frequencies, chiral solutions were obtained up to a certain value of ω, and all attempts to go higher caused the iterations to fall into a different minimum. This is probably due to multiple smooth crossings of occupied and empty levels, particularly in neutrons.

The HF results presented so far corroborate the main prediction of the classical model, that chiral solution exists only above a certain critical frequency, at which it branches off from the planar one. Also the intrinsic-frame trajectory of $\boldsymbol{\omega}$ along the HF chiral band is almost a straight line parallel to the medium axis, as in the classical case. This is demonstrated in Fig. 10, which shows projections of $\boldsymbol{\omega}$ on the s-m and
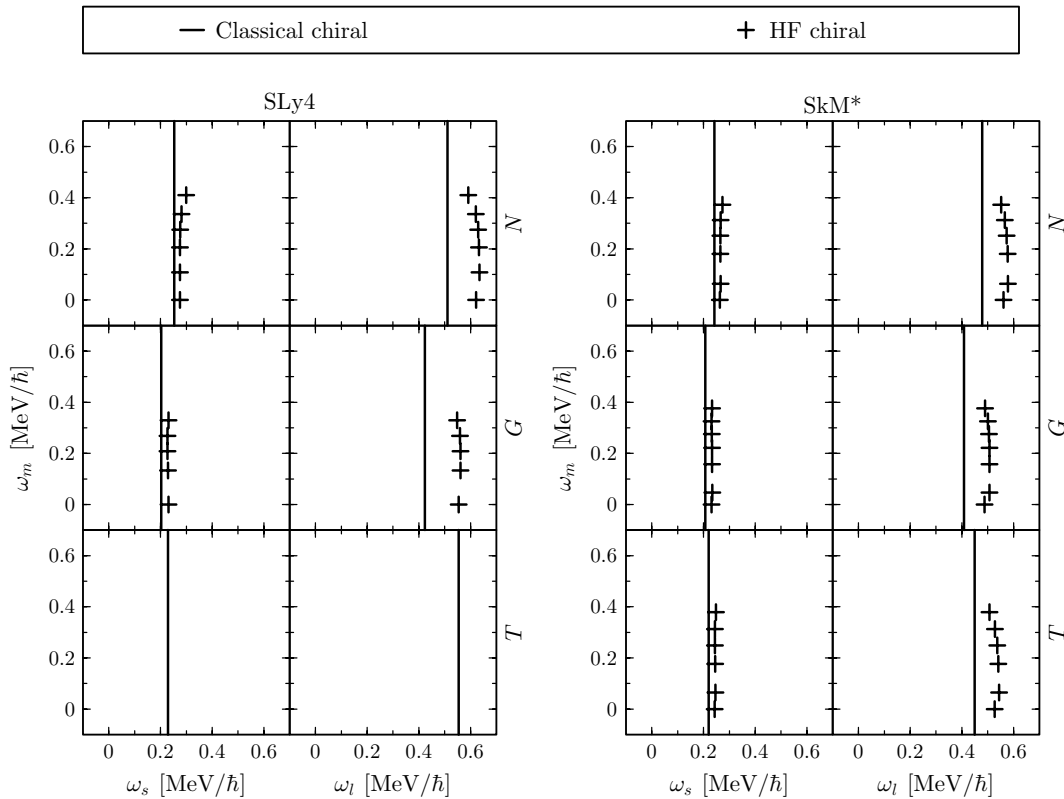

FIG. 10. Trajectories of the angular frequency vectors following the HF chiral bands in ^{132}La (plus symbols), compared to the classical solutions (solid lines). Projections onto the s-m and l-m planes of the intrinsic frame are shown. The HF results with the SLy4 and SkM* forces are shown for the N, G, and T variants of calculation defined in Sec. III B.

l-m intrinsic planes for the HF (plus symbols) and classical (line) results. The only difference is that $\omega_{\text{crit}}^{\text{HF}}$ is a bit higher than $\omega_{\text{crit}}^{\text{clas}}$, and the HF line is shifted along the planar band to higher frequencies. Although the chiral solutions have been found in a rather narrow ω interval, of about 0.1 MeV/$\hbar$, the accompanying increase in ω_m is significant, from zero to about 0.4 MeV/$\hbar$. This is so because ω_s and ω_l are relatively large and almost constant along the chiral solution.

Figure 6 shows the proton and neutron s.p. Routhians for the chiral solution obtained in ^{132}La with the SkM* force and no time-odd fields. A thin vertical line is drawn at the value of $\omega_{\text{crit}}^{\text{HF}}$. The Routhians to the left and to the right of this line correspond to the planar and chiral bands, respectively. Note first that the planar and chiral Routhians do indeed coincide at $\omega_{\text{crit}}^{\text{HF}}$. The chiral Routhians do not seem to exhibit any particular behavior. At high frequencies, the Routhian occupied by the neutron hole enters into a region of high level density and the corresponding s.p. state mixes with other negative-parity states. Thus, it is doubtful whether the valence neutron hole can be identified with a single state, and we do not examine its s.p. properties. The marking in open circles is only tentative. However, the $h_{11/2}$ proton particle is still well separated.

The alignments of the angular momentum $\boldsymbol{j}^p$ of the $h_{11/2}$ proton particle on the short, medium, and long intrinsic axes

for the SLy4 and SkM* forces and N, G, T time-odd fields are shown in Fig. 7. As in Fig. 6, the vertical line separates the planar and chiral bands. The plot confirms the stiff character of those alignments in the chiral solutions. Since the ω_s and ω_l components of the cranking-frequency vector hardly change along the chiral band, the considered alignments on those axes, j_s^p and j_l^p, are also nearly constant. Only the projection on the medium axis, j_m^p, increases owing to the increase in ω_m from zero to about 0.4 MeV/$\hbar$.

H. Separability of the TAC rotation

To complete the presentation of our results, we here formulate and discuss the separability rule, by which our planar (2D) and chiral (3D) HF TAC solutions turn out to be simple superpositions of independent HF PAC (1D) rotations about two or three principal axes, respectively.

Take, for instance, the total alignments on the principal axes, $I_i(\omega_i)$, where $i = s, m, l$, as functions of the corresponding components of the angular frequency. Such quantities were examined in Sec. III D for the PAC calculations, but they can be equally well extracted for the planar and chiral solutions. A comparison of the PAC and TAC results in ^{132}La is shown in the lower part of Fig. 11 for the T variant of calculations with the SkM* force. The PAC values of I_s, I_m, and I_l are plotted with
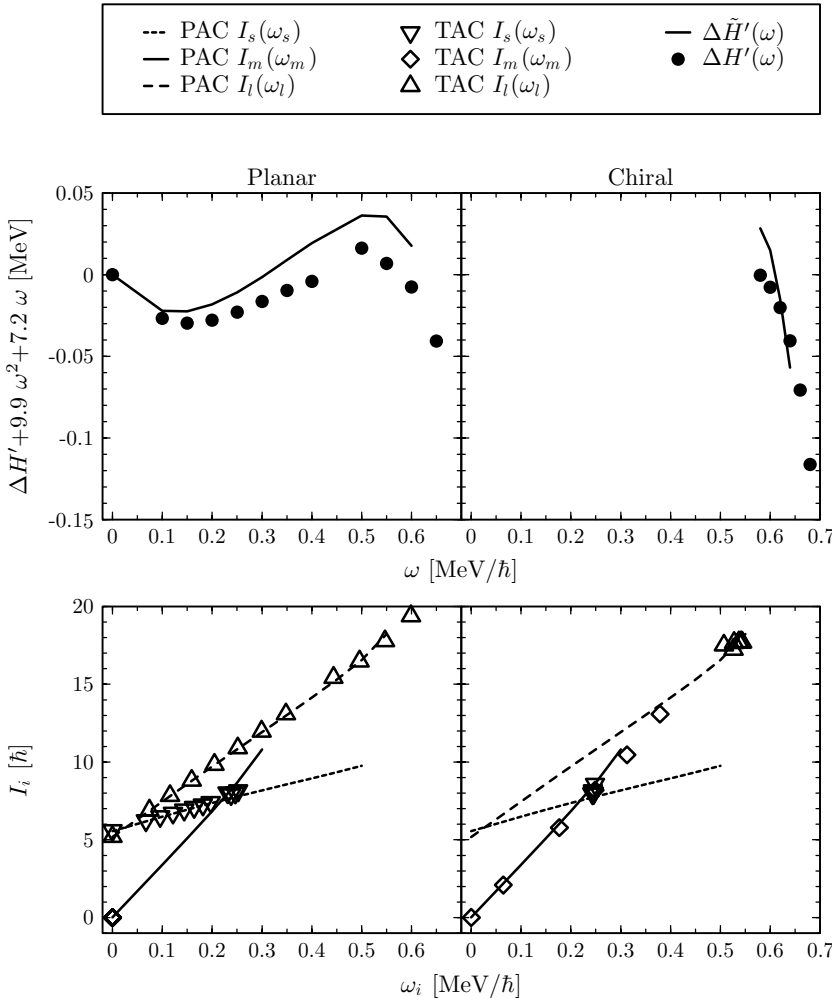

FIG. 11. Comparison of the full TAC (points) total angular momentum alignments (lower part) and Routhians (upper part) with analogous quantities obtained within the PAC approach, as discussed in the text (lines). The alignments I_i on the principal axes $i = s, m, l$ are shown as functions of the corresponding components ω_i of the angular frequency. The increments $\Delta H'$ (27) and $\Delta \tilde{H}'$ (26) in the full TAC and equivalent PAC Routhians with respect to $\omega = 0$ are plotted as a function of the total frequency ω. In the latter plots, a quadratic function of ω is added to stretch the scale. The HF results for the planar (left) and chiral (right) solutions in ^{132}La are shown for the T variant of the calculations (see Sec. III B) with the SkM* force.

dotted, solid, and dashed lines, respectively. The TAC results are marked with down triangles, diamonds, and up triangles, respectively. The left and right parts of the figure show the TAC values of $I_i(\omega_i)$ for the planar and chiral solutions, respectively. It is obvious that the results obtained for the rotation about tilted axes are almost identical to those obtained from the independent PAC calculations.

Unlike the angular momentum, the average value of the total TAC Routhian, $\langle \hat{H}' \rangle$ of Eq. (1), cannot be trivially decomposed into contributions from rotations about the three principal axes. Yet, for each TAC solution, characterized by an angular frequency ω, we have its three intrinsic components, ω_i, and we can consider a sum, $\tilde{H}'$, of the corresponding values of the PAC Routhians, $\langle \hat{H}'_i \rangle(\omega_i)$, that is,

$$\tilde{H}'(\omega) = \sum_{i=s,m,l} \langle \hat{H}'_i \rangle(\omega_i), \qquad (25)$$

which we call the *equivalent Routhian*. We then compare the difference relative to its value at $\omega = 0$,

$$\Delta \tilde{H}'(\omega) = \tilde{H}'(\omega) - \tilde{H}'(0), \qquad (26)$$

with the analogous difference,

$$\Delta H'(\omega) = \langle \hat{H}' \rangle(\omega) - \langle \hat{H}' \rangle(0), \qquad (27)$$

computed for the full TAC Routhian. In the upper part of Fig. 11, the differences (26) and (27) are plotted as a function of ω as lines and points, respectively.

For the chiral solution, as $\langle \hat{H}' \rangle(0)$ we take the same value as for the planar case, because the chiral band can be regarded as a continuation of the planar one, as discussed in Sec. III G. The equivalent Routhian can be plotted only in such a frequency range in which the PAC solutions are obtained for the corresponding components ω_i. In that range, $\Delta \tilde{H}'$ deviates from $\Delta H'$ by not more than 30 keV, as can be seen from the figure, whereas the total Routhian itself drops by about 8 MeV between $\omega = 0$ and 0.6 MeV/$\hbar$. Therefore, we conclude that the equivalent Routhian, constructed out of the PAC solutions, reproduces the full TAC Routhian to a very high accuracy.

Another piece of information contained in the TAC results, and not directly in the PAC results, is how the total angular frequency ω should be distributed over the three principal axes for each given point of a band representing the rotation about a tilted axis. That, however, can also be determined from the PAC solutions by means of the Kerman-Onishi requirement [37] (see Sec. II) that the angular momentum vector must be parallel to the angular frequency vector. Indeed, this condition is equivalent to the system of three nonlinear equations,

$$\begin{aligned} I_s(\omega_s)/\omega_s &= \mu, \\ I_m(\omega_m)/\omega_m &= \mu, \\ I_l(\omega_l)/\omega_l &= \mu. \end{aligned} \qquad (28)$$

By plotting the three PAC functions $I_i(\omega_i)/\omega_i$ on the same graph as functions of ω_i we obtain a planar or chiral solution whenever two or three, respectively, of these functions cross a horizontal line. Then, values of ω_i corresponding to the crossing points define the requested distribution of the components within the total angular frequency ω. The

agreement of the PAC and TAC alignments shown in Fig. 11 guarantees that this procedure gives a correct result.

We have thus demonstrated that, within our HF results, the general 2D or 3D rotation separates into two or three, in a sense independent, 1D rotations about the principal axes. This is possible mainly because our solutions are very stiff against deformation changes with rotational frequency. Had they been soft, rotations about different (principal or tilted) axes could cause different shape polarizations that would prevent such a simple superposition of motions. Yet, whenever the motions are separable, the PAC calculations supplemented with the Kerman-Onishi condition are actually sufficient to describe the 2D or 3D rotations. Although this rule has to be, in principle, confirmed numerically in each particular case, it is plausible that it will hold in all analogous cases of stiff alignments, by which the difficult TAC calculations can be replaced by much more easily performed PAC calculations.

IV. DISCUSSION

The main point left for the discussion concerns the values of the critical frequency: Where do they come from, whether they depend on the Skyrme force used, how they are altered by the different time-odd terms of the functional, how they would be influenced by the inclusion of pairing, and what their relation to the experimentally observed bands is. In this section we give some remarks on these and related topics.

Table I summarizes the values of the classical-model parameters, $\mathcal{J}_s$, $\mathcal{J}_m$, $\mathcal{J}_l$, s_s, and s_l, extracted from the HF PAC results in Sec. III D, of the classical critical frequency $\omega_{\text{crit}}^{\text{clas}}$, calculated from Eq. (22), and of the critical frequency $\omega_{\text{crit}}^{\text{HF}}$, obtained from the HF TAC calculations as defined in Sec. III G. In addition, the table gives the corresponding values of critical spins, $I_{\text{crit}}^{\text{clas}}$ and $I_{\text{crit}}^{\text{HF}}$, respectively.

First, it can be seen from the examples of ^{130}Cs and ^{132}La that the SLy4 and SkM* forces give quite similar values for all the concerned quantities. The differences are not larger than variations within one force because we take into account different time-odd fields. For all four isotones in question, switching on the fields G increases all the moments of inertia, but particularly $\mathcal{J}_m$, with respect to the case N. This causes a decrease in $\omega_{\text{crit}}^{\text{clas}}$, but the corresponding $I_{\text{crit}}^{\text{clas}}$ does not change much, because $\mathcal{J}_m$ is larger. Switching on the fields T results in values of $\mathcal{J}_m$ between those obtained for the cases N and G. The critical frequency always becomes higher than for the G fields, and the resulting critical spin is always the highest among all the examined sets of time-odd fields. These variations in $I_{\text{crit}}^{\text{clas}}$ are of the order of a few spin units.

In ^{132}La, where the HF chiral solutions were found in Sec. III G, values of the HF critical frequency and spin, $\omega_{\text{crit}}^{\text{HF}}$ and $I_{\text{crit}}^{\text{HF}}$, are slightly higher than the classical estimates, $\omega_{\text{crit}}^{\text{clas}}$ and $I_{\text{crit}}^{\text{clas}}$. This can be understood on the basis of results of the perturbative search for the HF chiral solutions, performed in Sec. III G. As illustrated in Fig. 9, the perturbative ratio I_m/ω_m, representing the moment of inertia with respect to the medium axis, $\mathcal{J}_m$, slightly falls with rotational frequency, which, according to Eq. (22), causes the rise of the critical frequency. When the time-odd fields are included, values of $\omega_{\text{crit}}^{\text{HF}}$ and $I_{\text{crit}}^{\text{HF}}$ vary similarly to those of $\omega_{\text{crit}}^{\text{clas}}$ and $I_{\text{crit}}^{\text{clas}}$.

The HF method used in the present study does not take into account the pair correlations. To include pairing in self-consistent calculations one would have to apply the Hartree-Fock-Bogolyubov (HFB) method in the TAC regime with two quasiparticle states blocked. Present codes do not allow for such a study, and a systematic investigation of pairing has to be left for future analyses. Convergence in the presence of blocked states may be more difficult to obtain. Pairing may soften the quasiparticle alignments and render the solution more prone to deformation changes. It remains to be seen how this would influence the pure single-particle picture that we have examined so far. Supposing that the HFB TAC results can be inferred from the HFB PAC calculations through a determination of the parameters of the classical model, one could gain some information on pairing effects by analyzing the HFB PAC moments of inertia and alignments.

The critical frequency represents the transition point between planar and chiral rotation. The notion of critical frequency was first introduced in Ref. [32], where the expression (22) for its value was derived from the simple classical model presented in Sec. III E. However, the occurrence of a transition from planar to chiral regime in the structure of chiral bands was clear already from earlier investigations. Both within the PRM and TAC, this effect was obtained numerically but left without comment. This transition is abrupt in the semiclassical cranking model, but it may be rather smooth in real nuclei. This is because the angular momentum vector oscillates about the planar equilibrium below ω_{crit}, which corresponds to nonuniform classical rotations [23], whereas above ω_{crit}, it can still tunnel between the left and right chiral minima, which represents chiral vibrations [2].

For these reasons, mean-field methods can provide a quantitative description of the bands in question only in the low-spin, planar regime, where there is only one minimum. In the chiral region, the mean-field approach does not take into account the interaction between the left and right minima, which are exactly degenerate in energy, and the experimentally observed energy splitting between the chiral partners cannot be calculated. It is argued in the literature that the mean-field chiral solution can be viewed as a kind of average of the two partner bands, and thus mean trends can be compared. One can also speculate about the value of the critical frequency or spin. Describing the transition region is an interesting topic for study and invokes techniques beyond the mean field, such as the generating-coordinate method.

Figure 1 gives a comparison of experimental and calculated energies in ^{132}La. Full symbols denote the experimental yrast (circles), B1 (squares), and B3 (diamonds) bands, discussed in Sec. III B. Open circles and black crosses represent the HF TAC planar and chiral solutions, respectively. Their classical counterparts are marked with dashed and solid lines. The HF results for the critical spin, $I_{\mathrm{crit}}^{\mathrm{HF}} = (17.8-20.3)\hbar$, are rather high compared to the spin range, in which the bands B1 and B3 are observed. Yet, the classical estimate, $I_{\mathrm{crit}}^{\mathrm{clas}} = 9.2\hbar$, evaluated for the total-Routhian-surface (TRS) [44] PAC results is already below that range [32]. This means that the inclusion of pairing in the calculations may be important for correct interpretation of the data. However, from the closeness of experimental spins to the possible values of I_{crit} one

can suppose that, whichever of the bands B1 and B3 could eventually be interpreted as the chiral partner of the yrast band, the concerned spin region may actually represent the transition between planar and chiral rotation. Although no HF chiral solutions were found in ^{130}Cs, similar conclusions can be drawn for that isotone on the basis of the classical estimates of the critical spin. For ^{134}Pr and ^{136}Pm it is not clear whether the *oblate* or *triaxial* solutions should be taken for comparison with the bands observed in those nuclei.

At low spins in ^{132}La, where the supposed chiral partners have not been observed, the yrast band is well reproduced by the HF planar solutions, particularly with the time-odd fields included. This is consistent with the supposed planar character of rotation at low spins. Roughly at the spin where the chiral partners commence to be visible, the yrast band significantly changes its behavior, which can be attributed to entering into the chiral regime. In this spin region the HF results agree semiquantitatively with experimental energies.

V. SUMMARY

In conclusion, the first Skyrme-Hartree-Fock calculations with the tilted-axis cranking were performed in ^{130}Cs, ^{132}La, ^{134}Pr, and ^{136}Pm to search for self-consistent solutions corresponding to nuclear chiral rotation. Only the configuration $\pi h_{11/2}^{1} \, \nu h_{11/2}^{-1}$, earlier assigned to the observed candidate chiral bands in those isotones, was considered. Two Skyrme parametrizations, SLy4 and SkM*, were used. Terms depending on time-odd nucleonic densities were either kept or excluded from the Skyrme energy functional.

From the principal-axis-cranking analysis it was concluded that the system in question can be modeled by two gyroscopes, representing the valence particle and hole, with spins stiffly aligned with the short and long axes of a triaxial rigid rotor, which stands for the core. Such a model was analyzed in the classical framework. This led to an important conclusion that chiral rotation can exist only above a critical angular frequency, given by a simple expression.

The HF solutions representing planar rotation were found in all the considered $N = 75$ isotones, and chiral solutions were obtained in ^{132}La. These solutions provide the first proof based on fully self-consistent methods that nuclear rotation can attain a chiral character. In all cases, the self-consistent solutions agree surprisingly well with the results of the classical model, which means that the model faithfully represents salient features of the examined phenomenon.

It was found that the time-odd densities in the energy functional have no qualitative influence on the results, but change mainly the moments of inertia. The HF values of the critical frequency are rather high compared to the spin range in which the candidate chiral bands were observed in ^{132}La. The HF energies agree satisfactorily with experiment only in the low-spin parts of the bands, where the rotation is supposed to be planar. In the chiral regime, the mean field is unable to reproduce the data precisely, and the agreement is only qualitative. It seems, also, that the experimentally observed bands actually represent a transition from planar to chiral rotation.

The criteria used so far when attributing the chirality-partnership interpretation to the experimentally found rotational bands that are based on the "small energy splitting" argument are clearly unsatisfactory in the long run. Numerous superdeformed band studies (followed by the normal-deformation studies) have shown that different intrinsic configurations and thus strictly speaking different-shape nuclei may manifest nearly identical rotational bands. It is therefore necessary to measure electromagnetic transition probabilities in a addition to the level energies. This could help exclude the mistake of interpreting, for example, the shape coexistence phenomena in terms of chirality—without providing extra sufficient conditions. In this paper we were not able to propose any clear-cut necessary-and-sufficient condition criteria to attribute the chirality label to the experimental bands either. However, we do believe that the concept of the critical frequency discussed in detail in this paper provides a useful tool in interpreting the experimental results. The very fact that in some nuclei the self-consistent HF calculations do provide chiral solutions is highly nontrivial and a very encouraging message in this field of research.

APPENDIX: ROTATIONAL PROPERTIES OF SINGLE-PARTICLE STATES IN A D_2^T-SYMMETRIC POTENTIAL

In this Appendix, we discuss elementary rotational properties of s.p. eigenstates of a mean-field Hamiltonian, which is symmetric with respect to the D_2^T group. The group D_2^T comprises the time-reversal operation $\hat{T}$, three signature operations $\hat{R}_x$, $\hat{R}_y$, $\hat{R}_y$, which are rotations through 180° about the three Cartesian axes, and products of the time-reversal and signature operations, which are called T signatures (cf. Ref. [45] for more information about this group in the context of mean-field calculations). In most cranking solutions corresponding to quadrupole deformation, the group D_2^T is a symmetry group of the s.p. Hamiltonian $\hat{h}$ of Eq. (3). For a single Kramers pair in a fixed potential, we investigate the response of the s.p. angular momenta to a cranking frequency applied in an arbitrary direction. Our conclusions are based only on symmetry arguments, and are thus independent of the particular implementation of the mean field.

Irrespective of spatial symmetries, whenever the s.p. Hamiltonian is invariant under time reversal, its spectrum exhibits the twofold Kramers degeneracy. We consider a single Kramers pair, whose states are denoted as $|\mu\rangle$ and $|\bar{\mu}\rangle$, where

$$\hat{T}|\mu\rangle = s_\mu|\bar{\mu}\rangle, \quad \hat{T}|\bar{\mu}\rangle = s_{\bar{\mu}}|\mu\rangle; \tag{A1}$$

s_μ is an arbitrary phase factor and $s_{\bar{\mu}} = -s_\mu$.

All information about the matrix elements of the angular momentum operator $\hat{J}$ between the states $|\mu\rangle$ and $|\bar{\mu}\rangle$ can be represented in a convenient way in terms of the real *alignment vector* J^μ and the complex *decoupling vector* D^μ of the state $|\mu\rangle$. They are defined as

$$J^\mu = \langle\mu|\hat{J}|\mu\rangle, \quad D^\mu = \langle\mu|\hat{J}|\bar{\mu}\rangle. \tag{A2}$$

Although the components of the decoupling vector change their phases when $|\mu\rangle$ and $|\bar{\mu}\rangle$ change theirs, the relative phases of those components do not depend on the phase convention. Since the angular momentum operator is odd under time reversal, it can be easily verified that

$$J^{\bar{\mu}} = \langle\bar{\mu}|\hat{J}|\bar{\mu}\rangle = -J^\mu, \quad D^{\bar{\mu}} = \langle\bar{\mu}|\hat{J}|\mu\rangle = D^{\mu*}. \tag{A3}$$

If the s.p. Hamiltonian is symmetric with respect to the D_2^T group, it is possible to chose the states forming the Kramers pair as eigenstates of any of the three signature operators $\hat{R}_i$, where $i = x, y, z$, but only one at a time, because the signature operators do not commute among themselves; that is, for $i \neq j$

$$\hat{R}_i\hat{R}_j = \sum_{k=x,y,z} \epsilon_{ijk}\hat{R}_k. \tag{A4}$$

This results, respectively, in three formally different pairs, $(|\mu_i\rangle, |\bar{\mu}_i\rangle)$, which are just three different bases in the same two-dimensional eigenspace of $\hat{h}$.

We choose states $|\mu_i\rangle$ so that they correspond to eigenvalues $-i$ under the action of $\hat{R}_i$, whereas the eigenvalues of $|\bar{\mu}_i\rangle$ are $+i$. Multiplication rules (A4) allow us to easily express eigenstates $|\mu_x\rangle$, $|\bar{\mu}_x\rangle$, $|\mu_y\rangle$, and $|\bar{\mu}_y\rangle$ through linear combinations of eigenstates $|\mu_z\rangle$ and $|\bar{\mu}_z\rangle$. By fixing the relative phase between states $|\mu_z\rangle$ and $|\bar{\mu}_z\rangle$ we obtain the following expressions:

$$|\mu_x\rangle = \sqrt{\frac{-i}{2}}(|\mu_z\rangle + |\bar{\mu}_z\rangle), \tag{A5}$$

$$|\bar{\mu}_x\rangle = -\sqrt{\frac{i}{2}}(|\mu_z\rangle - |\bar{\mu}_z\rangle), \tag{A6}$$

$$|\mu_y\rangle = \sqrt{\frac{i}{2}}(|\mu_z\rangle + i|\bar{\mu}_z\rangle), \tag{A7}$$

$$|\bar{\mu}_y\rangle = \sqrt{\frac{-i}{2}}(i|\mu_z\rangle + |\bar{\mu}_z\rangle), \tag{A8}$$

where $\sqrt{i} = \exp(i\pi/4)$ and $\sqrt{-i} = \exp(-i\pi/4)$. These formulas allow us to write J^{μ_x}, D^{μ_x}, J^{μ_y}, and D^{μ_y} in terms of J^{μ_z} and D^{μ_z}, that is,

$$J^{\mu_x} = \text{Re}\, D^{\mu_z}, \tag{A9}$$

$$D^{\mu_x} = -i J^{\mu_z} - \text{Im}\, D^{\mu_z}, \tag{A10}$$

$$J^{\mu_y} = -\text{Im}\, D^{\mu_z}, \tag{A11}$$

$$D^{\mu_y} = J^{\mu_z} - i\text{Re}\, D^{\mu_z}. \tag{A12}$$

The fact that $|\mu_i\rangle$ and $|\bar{\mu}_i\rangle$ are eigenstates of $\hat{R}_i$, together with the transformation rules of the components $\hat{J}_j$ of the

angular momentum operator under the three signatures,

$$\hat{R}_i^+ \hat{J}_j \hat{R}_i = \begin{cases} +\hat{J}_j & \text{for } j = i, \\ -\hat{J}_j & \text{for } j \neq i, \end{cases} \quad \text{(A13)}$$

induces limitations on the components $J_j^{\mu_i}$ and $D_j^{\mu_i}$ of the alignment and decoupling vectors. Namely,

$$J_j^{\mu_i} = \begin{cases} \text{nonzero} & \text{for } j = i \\ 0 & \text{for } j \neq i, \end{cases} \quad \text{(A14)}$$

$$D_j^{\mu_i} = \begin{cases} 0 & \text{for } j = i \\ \text{nonzero} & \text{for } j \neq i. \end{cases} \quad \text{(A15)}$$

In other words, $\boldsymbol{J}^{\mu_i}$ is confined to the axis i and $\boldsymbol{D}^{\mu_i}$ to the plane perpendicular to that axis.

From these relations and for the eigenstates defined as in Eqs. (A5)–(A8), it follows that all the quantities $J_j^{\mu_i}$ and $D_j^{\mu_i}$ can be expressed through the three "diagonal" components $J_i^{\mu_i}$ of the alignment vector,

$$\boldsymbol{J}^{\mu_x} = \left(J_x^{\mu_x}, 0, 0 \right), \quad \boldsymbol{D}^{\mu_x} = \left(0, J_y^{\mu_y}, -i J_z^{\mu_z} \right), \quad \text{(A16)}$$

$$\boldsymbol{J}^{\mu_y} = \left(0, J_y^{\mu_y}, 0 \right), \quad \boldsymbol{D}^{\mu_y} = \left(-i J_x^{\mu_x}, 0, J_z^{\mu_z} \right), \quad \text{(A17)}$$

$$\boldsymbol{J}^{\mu_z} = \left(0, 0, J_z^{\mu_z} \right), \quad \boldsymbol{D}^{\mu_z} = \left(J_x^{\mu_x}, -i J_y^{\mu_y}, 0 \right). \quad \text{(A18)}$$

Thus, all the information about the angular momentum matrix elements within a Kramers pair in the spectrum of a D_2^T-symmetric s.p. Hamiltonian is contained in three real numbers, $J_x^{\mu_x}$, $J_y^{\mu_y}$, and $J_z^{\mu_z}$.

The symmetry group D_2^T itself does not impose any conditions on the "diagonal" components $J_i^{\mu_i}$. However, these values can be further restricted if some other symmetry is present. For example, if $\hat{h}$ is axially symmetric, say with respect to the z axis, then the states $|\mu_z\rangle$, $|\bar{\mu}_z\rangle$ are eigenstates of $\hat{J}_z$, which leads to quantization of $J_z^{\mu_z}$. In fact, $J_z^{\mu_z} = +1/2, -3/2, \ldots$, because $\hat{R}_z = \exp(-i\pi \hat{J}_z)$, whereas in the adopted convention $\hat{R}_z|\mu_z\rangle = -i|\mu_z\rangle$. For states $|\mu_x\rangle$ and $|\mu_y\rangle$, defined by (A5) and (A7), one easily finds

$$J_x^{\mu_x} = \tfrac{1}{2} \text{Re}\langle \mu_z | \hat{J}_+ + \hat{J}_- | \bar{\mu}_z \rangle, \quad \text{(A19)}$$

$$J_y^{\mu_y} = \tfrac{1}{2} \text{Re}\langle \mu_z | \hat{J}_+ - \hat{J}_- | \bar{\mu}_z \rangle, \quad \text{(A20)}$$

where $\hat{J}_+ = \hat{J}_x + i\hat{J}_y$ and $\hat{J}_- = \hat{J}_x - i\hat{J}_y$ are the ladder operators, which increment and decrement the magnetic quantum number J_z of an eigenstate $|J_z\rangle$ of $\hat{J}_z$,

$$\hat{J}_+|J_z\rangle \sim |J_z + 1\rangle, \quad \hat{J}_-|J_z\rangle \sim |J_z - 1\rangle. \quad \text{(A21)}$$

One can see, therefore, that the matrix elements in Eqs. (A19) and (A20) can be nonzero only if $|\mu_z\rangle$ and $|\bar{\mu}_z\rangle$ differ in J_z by one, that is, if $J_z^{\mu_z} = 1/2$. In such a case, $\langle \mu_z | \hat{J}_- | \bar{\mu}_z \rangle = 0$, and $J_x^{\mu_x} = J_y^{\mu_y}$. These results can be summarized as

$$\left(J_x^{\mu_x}, J_y^{\mu_y}, J_z^{\mu_z} \right) = \begin{cases} (J_\perp^{\mu_\perp}, J_\perp^{\mu_\perp}, J_\parallel^{\mu_\parallel}) & \text{for } J_\parallel^{\mu_\parallel} = 1/2, \\ (0, 0, J_\parallel^{\mu_\parallel}) & \text{for } J_\parallel^{\mu_\parallel} = 3/2, \ldots. \end{cases} \quad \text{(A22)}$$

The parameter

$$J_\perp^{\mu_\perp} = \tfrac{1}{2} \text{Re}\langle \mu_z | \hat{J}_+ | \bar{\mu}_z \rangle \quad \text{(A23)}$$

is not restricted by these kinematic conditions. It is related to the standard *decoupling parameter* $a = -2J_\perp^{\mu_\perp}$ considered by Bohr and Mottelson [14]. They take such phases for the states $|\mu_z\rangle$ and $|\bar{\mu}_z\rangle$ that the T signature y, $\hat{R}_y^T = \hat{T}\hat{R}_y$, is the complex conjugation in the basis formed by these states. Since $\hat{J}_+$ is even under $\hat{R}_y^T$, in that convention the matrix element in Eq. (A23) is real.

We now consider the TAC for a single Kramers pair in a D_2^T-symmetric potential. We make two simplifying assumptions; (1) that the Hamiltonian $\hat{h}$ in the Routhian $\hat{h}'$ of Eq. (3) does not change with rotational frequency (non-self-consistent cranking) and (2) that the considered Kramers pair has no coupling to other eigenstates of $\hat{h}$ through the angular momentum operator (isolated pair). The TAC under such conditions becomes a two-dimensional diagonalization problem, which can be solved analytically.

We use the basis of states $|\mu_z\rangle$ and $|\bar{\mu}_z\rangle$. For a degenerate Kramers pair, $\hat{h}$ reduces to its eigenvalue e. Matrix elements of the angular momentum operator are defined by Eq. (A18). Altogether, the matrix of the s.p. Routhian (3) takes the form

$$\hat{h}' = \hat{h} - \boldsymbol{\omega}\hat{\boldsymbol{J}}$$

$$= \begin{bmatrix} e & 0 \\ 0 & e \end{bmatrix} - \begin{bmatrix} \omega_z J_z^{\mu_z} & \omega_x J_x^{\mu_x} - i\omega_y J_y^{\mu_y} \\ \omega_x J_x^{\mu_x} + i\omega_y J_y^{\mu_y} & -\omega_z J_z^{\mu_z} \end{bmatrix}. \quad \text{(A24)}$$

It is easy to verify that the two eigenstates of this Routhian have opposite-sign mean angular momentum vectors $\boldsymbol{J}$, whose components read

$$J_i = \pm \frac{\omega_i \left(J_i^{\mu_i} \right)^2}{\left(\omega_x^2 \left(J_x^{\mu_x} \right)^2 + \omega_y^2 \left(J_y^{\mu_y} \right)^2 + \omega_z^2 \left(J_z^{\mu_z} \right)^2 \right)^{1/2}}. \quad \text{(A25)}$$

Equation (A25) constitutes the central point of discussion, because it defines the sought response of the s.p. angular momenta to rotation under the assumed conditions. Note that the dependence of J_i on ω_i is nonlinear in the general case.

Values of alignments (A25) are undefined if, and only if, all the products $\omega_i J_i^{\mu_i}$ vanish—in particular when $\omega = 0$. In such a case, the Routhian (A24) is proportional to unity, and the mean angular momenta of its eigenstates depend on their (arbitrary) unitary mixing.

Two extreme cases of the dependence (A25) deserve particular attention:

(i) If $J_x^{\mu_x} = J_y^{\mu_y} = J_z^{\mu_z} = g$, then $J_i = g\omega_i/\omega$, and $\boldsymbol{J}$ always orients itself along $\boldsymbol{\omega}$, already for infinitesimal ω. This can be dubbed *soft alignment*.

(ii) When only one of the parameters $J_x^{\mu_x}$, $J_y^{\mu_y}$, $J_z^{\mu_z}$ is nonzero, say $J_j^{\mu_j}$, then $J_i = J_j^{\mu_j}\delta_{ij}$, and $\boldsymbol{J}$ is independent of $\boldsymbol{\omega}$. We call this *stiff alignment* on the jth axis.

In axial nuclei, precisely one twofold degenerate substate of each deformation-split j shell has $J_\parallel^{\mu_\parallel} = 1/2$ and $J_\perp^{\mu_\perp} \neq 0$, which represents the soft alignment. According to Eq. (A22), all other necessarily have a vanishing decoupling parameter and are thus stiffly aligned with the symmetry axis. For prolate

shapes, the lowest energy substate has $J_\parallel^{\mu_\parallel} = 1/2$ and is soft, whereas for oblate shapes it is the highest substate. In triaxial nuclei, values of the parameters $J_i^{\mu_i}$, where $i = s, m, l$ corresponds to the short, medium, and long principal axes, are equal to the s.p. alignments obtained from the one-dimensional cranking about the three axes. Indeed, for cranking about the axis i, the s.p. states are eigenstates of $\hat{R}_i$. For example, from the results of Sec. III D, one can see that for the lowest $h_{11/2}$ substates of a triaxial nucleus only $J_s^{\mu_s}$ is nonzero, whereas for the highest substates only $J_l^{\mu_l}$ does not vanish. These alignments are thus stiff. Note that there are no states with stiff alignment on the medium axis. The response to rotation of the middle $h_{11/2}$ substates is soft, because all the three parameters, $J_s^{\mu_s}$, $J_m^{\mu_m}$, $J_l^{\mu_l}$, are nonzero.

In realistic cranking calculations the symmetry arguments discussed here interplay with the fact that there is angular momentum coupling between different Kramers pairs and that the mean field does change with rotational frequency. In the results of the present paper, however, the change of deformation induced by rotation is negligible. The angular momentum coupling of the lowest and highest $h_{11/2}$ substates to other s.p. states is rather weak, which can be seen from the small curvature of their one-dimensional Routhians in Fig. 2. The stiff character of their alignments is fully confirmed in our self-consistent calculations, as discussed in Sec. III D and further in the paper. Investigation on how suitable the notion of soft and stiff alignment is in other physical cases remains a subject for further research.

[1] S. Frauendorf and J. Meng, Nucl. Phys. **A617**, 131 (1997).

[2] K. Starosta, T. Koike, C. J. Chiara, D. B. Fossan, D. R. LaFosse, A. A. Hecht, C. W. Beausang, M. A. Caprio, J. R. Cooper, R. Krücken, J. R. Novak, N. V. Zamfir, K. E. Zyromski, D. J. Hartley, D. Balabanski, J.-Y. Zhang, S. Frauendorf, and V. I. Dimitrov, Phys. Rev. Lett. **86**, 971 (2001).

[3] C. M. Petrache, D. Bazzacco, S. Lunardi, C. Rossi Alvarez, G. de Angelis, M. De Poli, D. Bucurescu, C. A. Ur, P. B. Semmes, and R. Wyss, Nucl. Phys. **A597**, 106 (1996).

[4] S. Zhu, U. Garg, B. K. Nayak, S. S. Ghugre, N. S. Pattabiraman, D. B. Fossan, T. Koike, K. Starosta, C. Vaman, R. V. F. Janssens, R. S. Chakrawarthy, M. Whitehead, A. O. Macchiavelli, and S. Frauendorf, Phys. Rev. Lett. **91**, 132501 (2003).

[5] J. A. Alcántara-Núñez, J. R. B. Oliveira, E. W. Cybulska, N. H. Medina, M. N. Rao, R. V. Ribas, M. A. Rizzutto, W. A. Seale, F. Falla-Sotelo, K. T. Wiedemann, V. I. Dimitrov, and S. Frauendorf, Phys. Rev. C **69**, 024317 (2004).

[6] J. Timár, P. Joshi, K. Starosta, V. I. Dimitrov, D. B. Fossan, J. Molnar, D. Sohler, R. Wadsworth, A. Algora, P. Bednarczyk, D. Curien, Zs. Dombradi, G. Duchêne, A. Gizon, J. Gizon, D. G. Jenkins, T. Koike, A. Krasznahorkay, E. S. Paul, P. M. Raddon, G. Rainovski, J. N. Scheurer, A. J. Simons, C. Vaman, A. R. Wilkinson, L. Zolnai, and S. Frauendorf, Phys. Lett. **B598**, 178 (2004).

[7] E. Grodner, J. Srebrny, Ch. Droste, T. Morek, A. Pasternak, and J. Kownacki, Int. J. Mod. Phys. E **13**, 243 (2004).

[8] E. Grodner, I. Zalewska, T. Morek, J. Srebrny, Ch. Droste, M. Kowalczyk, J. Mierzejewski, M. Sałata, A. A. Pasternak, J. Kownacki, M. Kisieliński, A. Kordyasz, P. Napiorkowski, M. Wolińska, S. G. Rohoziński, R. Kaczarowski, W. Płóciennik, E. Ruchowska, A. Wasilewski, and J. Perkowski, Int. J. Mod. Phys. E **14**, 347 (2005).

[9] J. Srebrny, E. Grodner, T. Morek, I. Zalewska, Ch. Droste, J. Mierzejewski, A. A. Pasternak, J. Kownacki, and J. Perkowski, Acta Phys. Pol. B **36**, 1063 (2005).

[10] T. Koike, K. Starosta, C. J. Chiara, D. B. Fossan, and D. R. LaFosse, Phys. Rev. C **67**, 44319 (2003).

[11] J. Peng, J. Meng, and S. Q. Zhang, Phys. Rev. C **68**, 044324 (2003).

[12] K. Starosta, C. J. Chiara, D. B. Fossan, T. Koike, T. T. S. Kuo, D. R. LaFosse, S. G. Rohoziński, Ch. Droste, T. Morek, and J. Srebrny, Phys. Rev. C **65**, 044328 (2002).

[13] A. S. Davydov and G. F. Filippov, Nucl. Phys. **8**, 237 (1958).

[14] A. Bohr and B. R. Mottelson, *Nuclear Structure* (Benjamin, New York, 1975).

[15] S. Frauendorf, Nucl. Phys. **A557**, 259c (1993).

[16] S. Frauendorf, Nucl. Phys. **A677**, 115 (2000).

[17] S. Frauendorf, Rev. Mod. Phys. **73**, 463 (2001).

[18] H. Frisk and R. Bengtsson, Phys. Lett. **B196**, 14 (1987).

[19] S. Frauendorf, Z. Phys. A **358**, 163 (1997).

[20] V. I. Dimitrov, S. Frauendorf, and F. Dönau, Phys. Rev. Lett. **84**, 5732 (2000).

[21] S. Frauendorf, Acta Phys. Pol. B **32**, 2661 (2001).

[22] S. Frauendorf, Nucl. Phys. **A752**, 203c (2005).

[23] V. Dimitrov, F. Dönau, and S. Frauendorf, AIP Conf. Proc. **656**, 151 (2003).

[24] A. A. Hecht, C. W. Beausang, K. E. Zyromski, D. L. Balabanski, C. J. Barton, M. A. Caprio, R. F. Casten, J. R. Cooper, D. J. Hartley, R. Krücken, D. Meyer, H. Newman, J. R. Novak, E. S. Paul, N. Pietralla, A. Wolf, N. V. Zamfir, J.-Y. Zhang, and F. Dönau, Phys. Rev. C **63**, 051302(R) (2001).

[25] G. Rainovski, E. S. Paul, H. J. Chantler, P. J. Nolan, D. G. Jenkins, R. Wadsworth, P. Raddon, A. Simons, D. B. Fossan, T. Koike, K. Starosta, C. Vaman, E. Farnea, A. Gadea, Th. Kroll, R. Isocrate, G. de Angelis, D. Curien, and V. I. Dimitrov, Phys. Rev. C **68**, 024318 (2003).

[26] V. I. Dimitrov, F. Dönau, and S. Frauendorf, Phys. Rev. C **62**, 24315 (2000).

[27] E. Chabanat, P. Bonche, P. Haensel, J. Meyer, and R. Schaeffer, Nucl. Phys. **A627**, 710 (1997).

[28] J. Bartel, P. Quentin, M. Brack, C. Guet, and H.-B. Håkansson, Nucl. Phys. **A386**, 79 (1982).

[29] J. Dobaczewski and J. Dudek, Comput. Phys. Commun. **102**, 166 (1997); **102**, 183 (1997); **131**, 164 (2000).

[30] J. Dobaczewski and P. Olbratowski, Comput. Phys. Commun. **158**, 158 (2004); **167**, 214 (2005).

[31] J. Dobaczewski, J. Dudek, and P. Olbratowski, nucl-th/0501008 (2005).

[32] P. Olbratowski, J. Dobaczewski, J. Dudek, and W. Płóciennik, Phys. Rev. Lett. **93**, 052501 (2004).

[33] R. D. Woods and D. S. Saxon, Phys. Rev. **95**, 577 (1954).

[34] S. G. Nilsson, Mat. Fys. Medd. Dansk. Vid. Selsk. **29**, 16 (1955).

[35] V. M. Strutinsky, Nucl. Phys. **A122**, 1 (1968).

[36] V. M. Strutinsky, Nucl. Phys. **A95**, 420 (1967).

[37] A. K. Kerman and N. Onishi, Nucl. Phys. **A361**, 179 (1981).

[38] J. Timár, D. Sohler, B. M. Nyakó, L. Zolnai, Zs. Dombrádi, E. S. Paul, A. J. Boston, C. Fox, P. J. Nolan, J. A. Sampson, H. C. Scraggs, A. Walker, J. Gizon, A. Gizon, D. Bazzacco, S. Lunardi, C. M. Petrache, A. Astier, N. Buforn, P. Bednarczyk, and N. Kintz, Eur. Phys. J. A **16**, 1 (2003).

[39] S. P. Roberts, T. Ahn, K. Starosta, T. Koike, C. J. Chiara, and C. Vaman, Phys. Rev. C **67**, 057301 (2003).

[40] D. J. Hartley, L. L. Riedinger, M. A. Riley, D. L. Balabanski, F. G. Kondev, R. W. Laird, J. Pfohl, D. E. Archer, T. B. Brown, R. M. Clark, M. Devlin, P. Fallon, I. M. Hibbert, D. T. Joss, D. R. LaFosse, P. J. Nolan, N. J. O'Brien, E. S. Paul, D. G. Sarantites, R. K. Sheline, S. L. Shepherd, J. Simpson, R. Wadsworth, J.-Y. Zhang, P. B. Semmes, and F. Dönau, Phys. Rev. C **64**, 031304(R) (2001).

[41] K. Starosta, T. Koike, C. J. Chiara, D. B. Fossan, and D. R. LaFosse, Nucl. Phys. **A682**, 375c (2001).

[42] J. Dobaczewski and J. Dudek, Phys. Rev. C **52**, 1827 (1995).

[43] H. Goldstein, *Classical Mechanics* (Addison-Wesley, Cambridge, 1953).

[44] W. Satuła and R. Wyss, Phys. Rev. C **50**, 2888 (1994).

[45] J. Dobaczewski, J. Dudek, S. G. Rohoziński, and T. R. Werner, Phys. Rev. C **62**, 014310 (2000); **62**, 014311 (2000).